Characteristic measurements of a hybrid pixel detector

Master's thesis, 22.11.2021

Author:

Vesa Ihanainen

Supervisor:

Arttu Miettinen
Janne Yliharju

JYVÄSKYLÄN YLIOPISTO
FYSIIKAN LAITOS

Tiivistelmä

Vesa Ihanainen
Characteristic measurements of a hybrid pixel detector
Pro-gradu -tutkielma
Fysiikan laitos, Jyväskylän yliopisto, 2015, 68 sivua

Tässä tutkielmassa otan käyttöön ja karakterisoin fysiikan laitokselle hankitun energiasensitiivisen röntgenkameran Advacam WidePix L 1x10. Hankinnan tarkoituksena on mahdollistaa energiasensitiivinen kuvantaminen. Kameran karakterisoitavaksi ominaisuuksiksi valitsin energiaresoluution, paikkaresoluution, kynnysten kohinareunan ja fotonien laskentanopeuden. Mittausten tulokset ovat lähellä valmistajan ilmoittamia arvoja, sekä aiemmin tehtyjä mittauksia Medipix 3RX -siruista. Kamerasta löytyi ongelma, sillä energiaresoluution määrityksessä huomasin pikseleiden välillä olevan huomattavia eroja amerikium-241 radioisotoopin 59.5409 keV röntgenpiikin energiassa.

Avainsanat: röntgenilmaisimet, karakterisointi, fotonien laskenta, energiaresoluutio, paikkaresoluutio

Abstract

Vesa Ihanainen
Characteristic measurements of a hybrid pixel detector
Master's thesis
Department of Physics, University of Jyväskylä, 2021, 68 pages.

In this thesis, I commissioned and characterized a photon counting x-ray camera for the complex materials research group. The camera Advacam WidePix L 1x10 is a new device for the group and for the Physics Department of University of Jyväskylä. The intention for acquiring the new camera was to enable energy sensitive tomography. I chose energy resolution, spatial resolution, photon counting speed and the noise edge of the energy thresholds as characteristics to be measured and determined from the camera. The measured values agrees with the measurements done on the Medipix 3RX chip which is the base of the acquired camera. The measurements also agrees with the specificiations given by the manufacturer. However, I found out that the energy resolution varies from pixel to pixel. This discrepancy was when measuring the characteristic 59.5409 keV X-ray peak of Americium-241. The ultimate reason for this discrepancy wasn't found but it is likely due to imperfect pixel-wise energy calibration of the camera.

Keywords: x-ray detectors, characteristic measurements, photon-counting, energy resolution, spatial resolution

Contents

1 Introduction

Recently, a new generation of X-ray cameras have been developed. These new generation cameras can determine the energy of incoming x-ray photons which enables energy sensitive imaging. Energy resolving cameras enable new possibilities for x-ray imaging, for example material decomposition. Material decomposition can be used to determine which materials make up the sample. Another use for energy sensitive cameras is medical imaging in which the cameras enables better diagnostics and reduced x-ray doses.

Energy resolving cameras can be, for example, realized by counting photons. Photon counting detectors can be constructed using a hybrid detector configuration, where an application specific integrated circuit (ASIC) is combined with semiconductor sensor.

The idea in the photon counting detector is to count the number of incoming photons in an energy range or all photons over certain energy threshold(s). This gives an advantage in energy resolution compared to determination of energies of the incoming x-ray photons directly. The advantage in the energy resolution with photon counting is that the error depends on the error of the energy thershold(s). So there isn't need to determine error for measurement of the energy of each and every photon but to determine the error in the energy threshold itself.

In this thesis, an Advacam photon counting detector based on the chips by the Medipix CERN collaboration is commissioned and characterized. The history of Medipix energy resolving ASICs began by release of the first chip in 1997. Since then two generations of Medipix chips have been released in 2005 and 2013 which can be used in industrial or medical energy resolving x-ray imaging. The improvements in these generations were tileability from 3 sides and charge summing mode which enables more efficient usage of high z-sensors. The fourth generation of Medipix chips is under developement as of writing this thesis.

The characteristics chosen to be determined were energy resolution, spatial resolution, noise edge on thresholds and the photon counting speed. Energy and spatial resolutions were obvious choices for characteristics to be measured as they

have an important role in x-ray tomography. The noise edge on thresholds was chosen as the lowest possible usable energy threshold, and it has to be known when planning imaging. For the same reason, the photon counting speed was chosen to be characterized as it directly relates to the maximum photon flux that can be used for imaging.

In the literature, there are measurements of the performance of Medipix 3RX chips similar to those in the Advacam camera used in this thesis. Due to the chips being provided by different manufacturers and somewhat unusual configuration of 10 Medipix 3RX chips with 55 µm pixel pitch with 1 mm Cadmium-Telluride, the measurements in the literature aren't directly applicable for this camera but can be used to gauge the performance of the camera. Due to the number of chips the differences between chips weren't considered in all the measurements as this proved to be cumbersome.

This thesis begins with brief introduction to x-ray imaging which covers x-ray interaction with material, x-ray sources and x-ray detectors. After the introduction to x-ray imaging, the thesis continues with detailed descriptions of the photon counting detector used in the thesis, the measurement setups and the results.

2 X-ray imaging

X-ray imaging requires three objects: the x-ray source, the object to be imaged and the x-ray camera. This section begins with an introduction to interaction between x-rays and material as this plays an important part in the whole operating principle of the x-ray camera. After the introduction to interactions the section continues with description of x-ray sources and typical x-rays cameras and photon counting detectors.

2.1 X-ray interaction with material

The foundation of x-ray tomography is the inversion of the Beer-Lambert's law which describes how x-ray attenuates inside of a material. In inversion problems one has measured a set of observations, in this case the intial beam intensity and the beam intensity after being attenuated, and one calculates the causal factors that produced the set of observation. Basically inverting the measurement to determine the causal factors leading to the measured result.

The Beer-Lambert's law describes an inversion problem for the attenuation coefficients of the material in terms of initial beam intensity and the beam intensity after being attenuated inside of the material. The attenuation of x-rays inside of a material is a result of interaction processes. There are many processes leading to attenuation of x-rays inside of a material, for example Compton scattering and Photoelectric effect.

The most important interactions for x-ray tomography occurs in the energy region of 1 keV to 100 keV which is the typical x-ray imaging window. We can see the photon cross-section of a Cadmium-Telluride (CdTe) plotted in figure 1. In the region 1 keV to 100 keV three types of interactions are possible. These are the Rayleigh or Thomson scattering, the Compton scattering and the photoelectric effect.

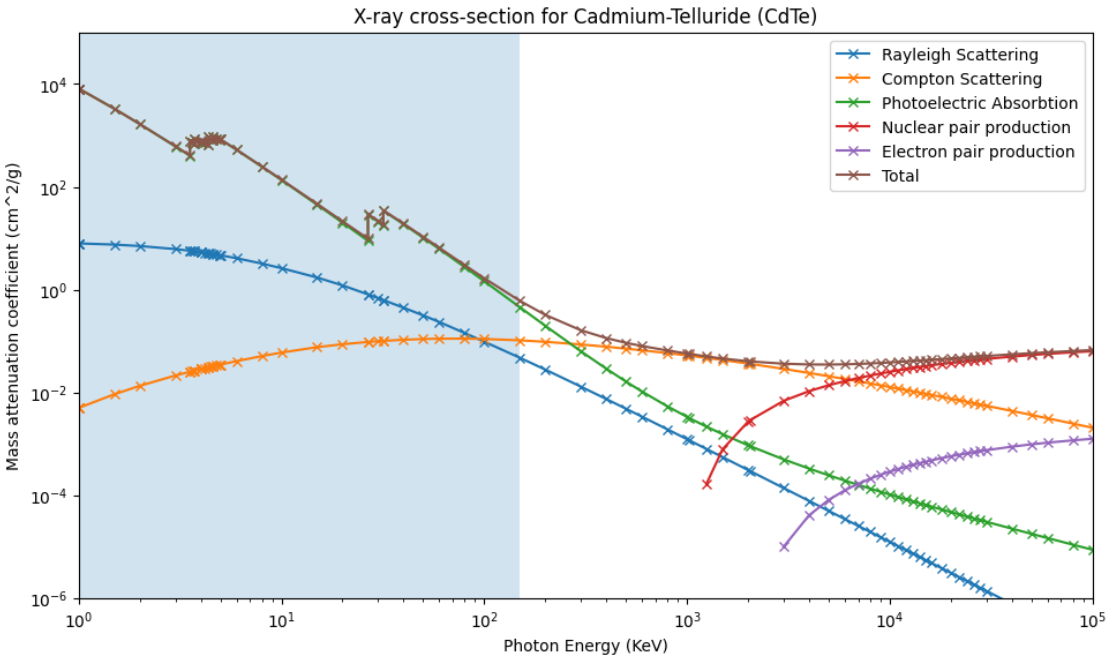

Figure 1. X-ray cross-section for Cadmium-Telluride (CdTe) with subdivision to the contributions of the most relevant interaction processes. The usual x-ray imaging range has been plotted in the image as light blue background. From the image it can be seen that the most dominant interaction is photoelectric absorption. (Figure: Vesa Ihanainen, 2020, Data: [1])

2.1.1 Beer-Lambert's law

The basis of tomography is Beer-Lambert's law which describes how x-ray attenuates inside of a material. Let's derive the Beer-Lambert's law in parallel beam geometry which means that there isn't any scattered radiation in the beam. In simplier terms the beam is like multiple parallel pencils pointing directly to the x-direction going through the object. Let's follow the path of a single x-ray photon to the detector.

The Beer-Lambert's law can be derived by inspecting radiation intensity inside of an object. Let's denote the intensity of radiation by I and assume that the x-ray beam is monochromatic, meaning that the beam has only single energy. After passing a distance Δx inside the object the intensity can be formulated as

$$I(x + \Delta x) = I(x) - \mu(x)I(x)\Delta x, \tag{1}$$

where $\mu(x)$ is the attenuation inside the object or the linear attenuation coefficient. Let's assume homogeneous material where μ doesn't vary as a function of x. We can

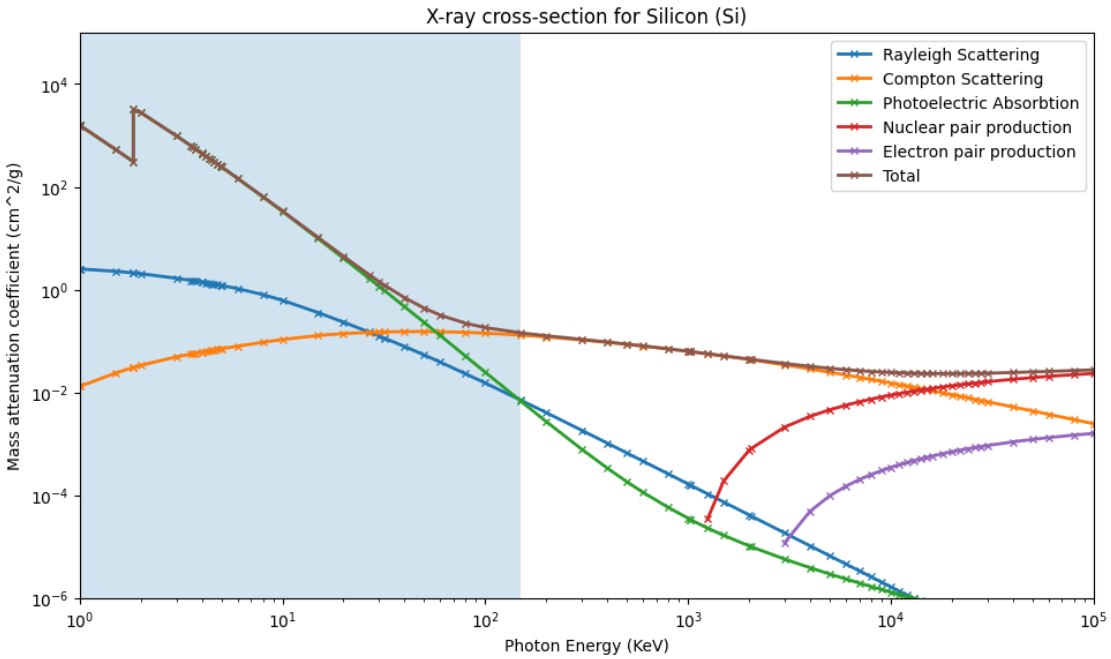

Figure 2. X-ray cross-section for Silicon (Si) with subdivision to the contributions of the most relevant interaction processes. Similary to Cadmium-Telluride the photoelectric absorption dominates up until 60 keV after which Compton scattering becomes dominant interaction. (Figure: Vesa Ihanainen, 2020, Data: [1])

reorder the equation (1) to get

$$\frac{I(x+\Delta x)-I(x)}{\Delta x} = -\mu I(x). \tag{2}$$

This can be written as a differential equation by taking limit $\Delta x \to 0$

$$\lim_{x\to 0} \frac{I(x+\Delta x)-I(x)}{\Delta x} = \frac{dI}{dx} = -\mu I(x). \tag{3}$$

The differential equation (3) can be solved and the solution is an exponential function

$$I(x) = \exp\left(-\mu x + C\right). \tag{4}$$

Because we have an implied initial condition that

$$I(0) = I_0. \tag{5}$$

Meaning that the intensity just before going inside of the object is I_0 the intensity produced by the x-ray source. Now we get

$$I(x) = I_0 \exp(-\mu x) \tag{6}$$

as the solution for (3). Tomography is an inverse problem where we have measured $\frac{I}{I_0}$ and we want to solve the attenuation coefficient $\mu(x)$ for every x for, typically, non-homogenous material. In typical case we don't have a perfect parallel geometry as there will be some scattered radiation and a point-like radiation source.

The attenuation coefficients vary inside of the non-homogenous material. This means that the attenuation coefficient μ varies with x in (6). We can modify the equation (6) by taking a path integral of the varying attenuation coefficients $\mu(x)$ along the path inside of the material. This results in the equation

$$I(x) = I_0 \exp\left(-\int_0^L \mu(x)\mathrm{d}x\right) \tag{7}$$

where L is the length of the material.

In the case of polychromatic radiation the I_0 is a function of the energy E of the x-rays. This means that essentially the initial intensity I_0 and the attenuation coefficients $\mu(x,E)$ are dependent on the energy of the x-rays. Taking this into account we can modify the (7) to

$$I(x) = \int_0^{E_{max}} \frac{\mathrm{d}I_0(E)}{\mathrm{d}E} \exp\left(-\int_0^L \mu(x,E)\mathrm{d}x\right) \mathrm{d}E. \tag{8}$$

The linear attenuation coefficient depends on the total photon atomic cross-section σ_{tot} which is dependent on the interaction processes with x-rays and the material. The dependency is defined as

$$\mu = \frac{\rho N_a}{A}\sigma_{\text{tot}} \tag{9}$$

where ρ is the density of the material, N_a is the Avogadro constant and A is the atomic weight of the material.

Because the focus of this thesis is in the photon counting detector, the equation (8) should be written in terms of photon count N. Let's define $S_0(E)$ as the distribution of number of photons emitted from the x-ray source. In the sense of Beer-Lambert's

law for polychromatic radiation, equation (8) can be written in terms of photon count distribution $S_0(E)$

$$N(x) = \int_0^{E_{max}} S_0(E) \exp\left(-\int_0^L \mu(x,E)\mathrm{d}x\right) \mathrm{d}E \tag{10}$$

where N is the total number photons after being attenuated by the object. With photon counting detectors, it is typically possible to select at least the minumum energy threshold for measurements. This means that in the equation (10) the integral begins from a set threshold value E_{th0}. The number of photons captured by ideal detector is

$$N(x) = \int_{E_{th0}}^{E_{max}} S_0(E) \exp\left(-\int_0^L \mu(x,E)\mathrm{d}x\right) \mathrm{d}E \tag{11}$$

if we choose $E_{th0} \neq 0$.

2.1.2 Rayleigh scattering

Rayleigh scattering is a coherent scattering process which involves photons and atomic bound electrons. After this scattering process the scattered photon has the same energy as the incident photon. In this proces, the energy transfer is negligible. There is no ionization occuring and the target atom doesn't get excited in the process. This means that the main effect is the change in the direction of the photon.

The differential cross-section of Rayleigh scattering can be approximated as

$$\frac{\mathrm{d}\sigma_R}{\mathrm{d}\Omega}(\theta) = \frac{r_0^2}{2}(1+\cos^2\theta)(F(q,Z)^2), \tag{12}$$

where σ_R is the Rayleigh cross-section, r_0 is the classical electron radius, θ is the photon scattering angle and $F(q,Z)$ is the atomic form factor. The atomic form factor is a function of recoil momentum q and atomic number Z. This means that the Rayleigh cross-section $\sigma_R \sim Z^2$. More details on how Rayleigh cross-sections are calculated can be found from [2] and [3].

2.1.3 Compton's scattering

The Compton's scattering was first observed by Compton in 1923 [4]. The scattering is an incoherent scattering process which involves incident radiaton (photons) and individual atomic electrons. The scattering process is an inelastic process but the kinematics of the reaction are of an elastic collision.

In the scattering process an incoming photon of momentum hv/c interacts with a quasifree electron at rest. This results in scattered photon with angle θ_v and an electron that recoils at an angle θ_e. The energy of the scattered photon depends on the photon scattering angle θ_v which is related to the incoming photon energy. The Compton Scattering process is shown in image 3

The differential Compton cross-section for unpolarized photons is the Klein-Nishina angular distribution

$$\frac{\mathrm{d}\sigma_c^{KN}}{\mathrm{d}\sigma} = \frac{1}{2} r_0^2 \left(\frac{k}{k_0}\right)^2 \left(\frac{k}{k_0} + \frac{k_0}{k} - \sin^2\theta_v\right) \tag{13}$$

where $k_0 = \frac{hv_0}{m_e c^2}$ is the reduced energy of the incoming photon and $k = \frac{hv}{m_e c^2}$. The equation (13) is good approximation when the energy of the photons are order of 1 MeV or higher. In order to calculate the Compton cross-section for lower photon energies a correction has to be added to the equation (13). This correction can be done using incoherent scattering function. The equation (13) becomes [3]

$$\frac{\mathrm{d}\sigma_c}{\mathrm{d}\theta} = S(q,Z)\frac{\mathrm{d}\sigma_c^{kn}}{\mathrm{d}\theta_v}. \tag{14}$$

For a more complete overview of calculation of Compton's cross section, the reader is advised to see [2] and [3].

Another interesting quantity that can be calculated from the Compton Scattering is the energy of the scattered photon. This can be derived using the very basic principles of physics: conservation of energy and momentum. The result is

$$E' = \frac{m_e c^2}{1 - cos(\theta_v + \frac{m_e c^2}{E})}, \tag{15}$$

where m_e is the mass of the electron, c is the speed of light, h is the Planck'constant and E is the energy of the incident photon. The angle θ_v in equation (15) is the scattering angle of photon as seen in figure 3. [5]

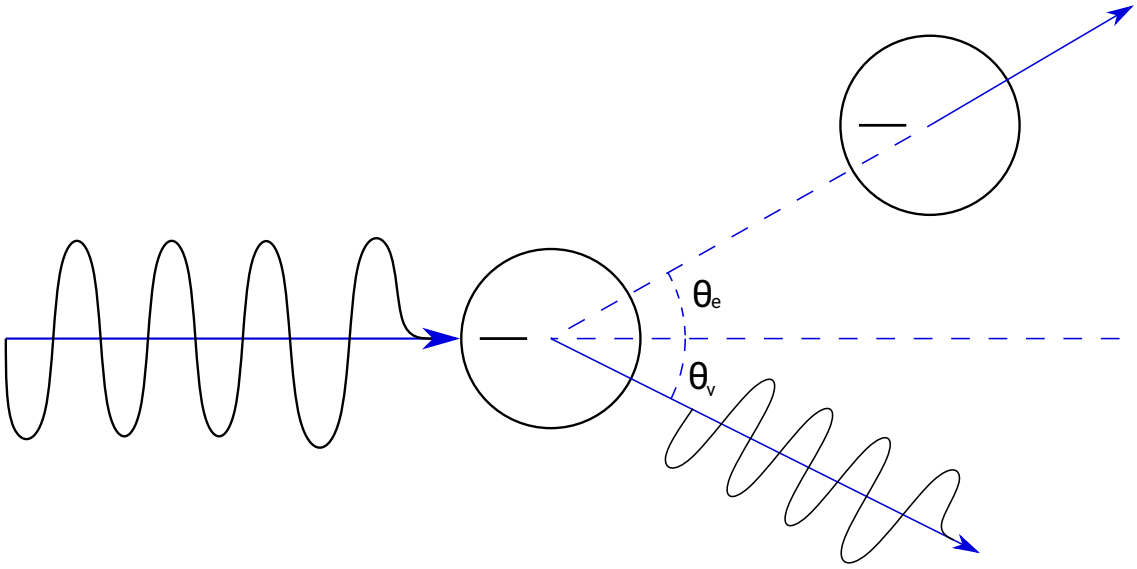

Figure 3. Sketch of Compton scattering process, where x-ray photon scatters from electron changing the direction of itself and the electron. (Figure: Vesa Ihanainen, 2021)

2.1.4 Photoelectric effect

The photoelectric effect is an interaction that involves a photon and an electron from the entire electron cloud of an atom.

A photon may be completely absorbed in the interaction with an atom if the photon's energy hv is higher than the binding energies B_e of the atomic electrons. If the photon is absorbed an electron raised to a state of the continuous spectrum is emitted. The kinetic energy E_k of the emitted electron is

$$E_k = hv - B_e. \tag{16}$$

If the energy of the incoming photon is higher than K-shell energies most of the photoelectric effect occurs with K-shell electrons. However, if the energy of the incoming photon is lower than the shell's binding energy electrons cannot be emitted from that shell. Therefore, there are absorption edges on the absorption spectrum of the substance. The energy where absorption edges appear coincides with the ionization energy of the electrons in the particular shells. [3]

2.1.5 Pair Production

The production of an electron and positron pair is possible when the photon energy of the incoming photon exceeds twice the energy corresponding to the electron rest mass.

The energy balance for electron-positron pair is given by

$$h\nu \rightarrow e^{-}e^{+}2E_{\text{kin}} \tag{17}$$

if the Einstein's mass-energy equivalency

$$h\nu = 2m_e c^2 + 2E_{\text{kin}} \tag{18}$$

is satisfied [3]. This means that the photon energy has to exceed $2m_e c^2 \approx 1.02\,\text{MeV}$ threshold. Due to high energy threshold required for pair production, this effect does not happen at the energies where x-ray imaging is done in this thesis.

2.2 X-ray sources

Most common x-ray sources for tomographic imaging are synchrotrons and x-ray tubes.

Synchrotrons are particle accelerators that can be used as light sources for synchrotron radiation. Synchrotron radiation is well suited for x-ray tomography as it has broad spectrum and high brilliance. The x-rays energy can be chosen more freely compared to x-ray tube.

The idea of x-ray tubes is to focus an electron beam onto a metal target. This causes the electrons to collide with the target and produces x-rays. The x-rays are produced from the strong interactions between electrons and the atoms of the metal target.

There are two sources of x-rays in x-ray tubes, Bremsstrahlung and characteristic radiation from the metal target. Bremsstrahlung is generated when electron interacts with the atomic nucleus and the electron decelerates. The excess energy gets emitted as a photon. The photon's upper limit of energy is the kinetic energy of the electron emitted from the electron gun.

Characteristic peaks in the x-ray spectrum depends on the target (anode) material of the x-ray tube. The characteristic peaks result from electron interaction with

the inner shell electrons of the anode material. Basically in the material inner shell electron gets ejected from the atom by the incoming electron beam from the electron gun. This creates a vacancy in the inner shell which is then filled by an outer shell electron. The excess energy is emitted as an x-ray photon with the same energy as the difference of the binding energy between the shells.

In the measurements I will be doing on this thesis, I will be using an x-ray tube and radioisotopes as the x-ray sources for the measurements.

2.3 X-ray detectors

This thesis focuses on the photon counting detector, however it is important to represent image sensor based detectors as this provides the required knowledge on why photon counting detectors have been developed and what are the advantages of the photon counting detectors. In this subsection I will cover the basics of both and in further section I will explain photon counting detectors in greater detail.

2.3.1 Image sensor based detectors

In an image sensor based detector an image sensor is typically coupled with a scintillator that absorbs incoming x-rays and emits the absorbed energy as light so that the image sensor can capture the light produced by the x-rays. This is since an image sensor based detector has an upper limit energy of 10 keV for the detection, meaning it can't detect high energy x-rays. There has been some development on direct detectors with higher upper energy limit but these are still limited to soft x-rays.

The working principle of an image sensor based detector is accumulating an electric charge that is proportional to the intensity of the incoming light like in a traditional digital camera. The electric charge is usually accumulated using metal-oxide-semiconductor (MOS) technology. There are two types of sensors based on the MOS technology those are charge-coupled device (CCD) which uses MOS capacitors and the Complementary Metal Oxide Semiconductor sensor (CMOS sensor) which is based on the MOS field-effect transistor (MOSFET) amplifiers and photodetectors.

CMOS sensors are prefered as CMOS chips are less expensive and can be read more rapidly and CMOS sensors use less power compared to CCD sensors. After the electrons have been accumulated in the sensor the individual pixels are read to a

readout register which is then transferred to mass storage.

To detect the x-ray photon in the sensor it must be turned into a light photon. This is done typically using scintillators. The scintillator is coupled to the image sensor using either a lens system or a fibre optic array. The lens system can be microscope-like turret configuration with multiple lenses. The coupling of the lens system can be done so that the scintillator or the lens and scintillator can be changed. For fibre optic array it isn't typically possible to change the fibre optic array easily as it is directly attached to the sensor.

The scintillator can be either organic or inorganic material. Organic scintillators are aromatic hydrocarbon compounds containing a benzenic cycle [3]. In organic scintillators, the process of converting x-ray photons to light photons is a two-step process. In the first step, the primary fluorescent material emits ultraviolet (UV) light after excitation and de-excitation in the molecular levels of the fluorescent material. This UV light must be shifted to visible light in a second fluorescent material whose absorption spectrum is matched with the emission spectrum of the primary fluorescent. The emission spectrum of the second fluorescent material should be matched with the quantum efficiency of the coupled detector. [3]

Inorganic scintillators are ionic crystals that might be doped with activators. The light photon is formed by electron returning from conduction band to the valence band after an x-ray excited the electron from valence band to conduction band forming a hole in the valence band. However, this is an inefficient process that can be improved by introducing an activator to the pure crystal. The activator has ground and excited states between the valence and conduction band (forbidden band) of the crystal. The added activator states between the valence and conduction band of the ionic crystal improve the probability of the light photon emission during the de-excitation process. The activator states form the basis for the scintillation process. [6]

After the incoming x-ray has been converted to a photon the photon needs to be converted to a measurable quantity namely voltage and electric current. Let's assume a p-type semiconductor for the next discussion.

It is possible for photons that hit and penetrate a semiconducting substrate to transfer part of their energy to the substrate. This happens by the generation of electron-hole pairs. Electron-hole pairs are generated when the energy of the incoming photon is high enough to release a photon from the valence band to the

conduction band. This leaves a hole in the valance band. The energy of the incoming photon is reduced by the band gap or the energy difference between conduction and valence band. For silicon the band gap is 1.1 eV or the wavelength has to be shorter than 1000 nm. [7] [8] However, the mean electron-hole creation energy is 3.66 eV higher than band gap [9].

After the electron-hole pairs have been generated in the substrate the next part is to separate the electrons from the holes. This is done by local integration where charge carriers are integrated into a charge packet which is then transported to the output. The integration is done by a small capacitor by junction capacitance in the bulk of the semiconductor [10]. [7]

Aforementioned CMOS sensors have become more common since 1997 as CMOS has lower power consumption and lower cost compared to CCD technology. Another major advantage is the possibility of integrating readout and signal processing electronics monolithically on the chip. [11].

The CMOS image sensor can have either active or passive pixels. The first CMOS sensors were passive pixels based on photodiodes [11] but active pixels (APS) became attractive as passive pixels suffered from low sensitivity and high noise[12]. Active pixel sensors have a per pixel amplifier which improves the performance of the pixel. Power dissipation remains low compared to CCDs in active pixels as the amplifiers are only turned on during readout. Photodiode type APS and photogate type APS are examples of active pixel CMOS sensors.

Direct x-ray imaging using CCD-cameras is possible but limited to soft x-rays. For example Hamamatsu offers three types of cameras for three energy ranges of 20 eV to 2 keV, 3 keV to 10 keV and above 10 keV [13]. Because of the soft x-ray limitation, these cameras are better for biological samples rather than samples containing heavier elements.

2.3.2 Photon counting detectors

Photon counting detector is a direct conversion detector in which the energy of the incoming x-ray photon is converted to an electric signal. As per the name in photon counting detectors the number of incoming photons are counted. Photon counting detectors can be designed so that they can bin the energy of the incoming x-ray photon between certain thresholds. This makes it possible to take energy-resolved images. In this thesis energy resolving photon counting detectors are the main focus.

Typically photon counting detectors are made by combining a semiconductor sensor usually Si, GaAs, or CdTe as in our case with an application-specific integrated circuit (ASIC) readout chip. For example Medipix 3, ASICs are bump bonded to the semiconductor sensor. In this design, the conversion of an x-ray photon to an electrical signal is direct because the conversion happens in the semiconductor sensor unlike in the case of CCD or CMOS sensors where a scintillator is required to convert an x-ray photon to a light photon which is then captured by the CCD or CMOS sensor.

When x-ray photon interacts with the semiconductor material of the sensor charge carriers are created in the semiconductor material. The movement of the charge carriers induces a current to the electrode of the semiconductor material. This induced current is what the ASIC processes and uses to count the number of photons in a certain energy bin with thresholds determined by the user. The induced current can be calculated using the Shockley-Ramo theory. The most notable outcome is that the current is induced as the charge carriers are moving to the electrode.

Silicon has many good properties for usage in high energy physics detectors namely homogeneity, availability and cost but for x-ray imaging, the problem with silicon is that the wafers made from silicon are thin and the absorption efficiency in the x-ray photon energy range 20 keV to 100 keV is low and decreases rapidly as seen in 2. This can be improved by using high-Z materials like the aforementioned GaAs and CdTe. There is a method to improve the absorption efficiency with silicon sensor by changing the geometry of the sensor to be edge-on instead of face-on geometry. This change in geomtery means that semiconductor is thicker in the direction of the x-rays.

Typical photon counting detector single-pixel readout consists of analog and digital circuitry. The analog circuitry consists of a charge sensitive amplifier and a shaper circuitry. The charge sensitive amplifier integrates the induced current from a single photon that hit the pixel. The shaper is a band-pass filter that is designed to improve the signal-to-noise ratio. The digital circuitry compares the output of the shaper circuit to the threshold(s) defined by the user and increments hit counter if the incoming photon energy is over the threshold. Note that energy binning must be done in post-processing.

3 Photon counting detectors in detail

Let's take a closer look at the signal formation in the typical photon counting detector consisting of a CdTe semiconductor sensor and readout electronics realized using charge sensitive amplifier and a shaper circuitry.

When an x-ray hits the semiconductor sensor there is a probability for it to interact with the sensor material. Absorption efficiency determines this probability. If this interaction happens the x-ray photon deposits a fraction (or all) of its energy to the volume of the sensor. The two most likely interactions are either photoelectric effect or Compton scattering. Especially for the CdTe sensor, the photoelectric effect is the most dominant interaction in the typical x-ray imaging window. For silicon, the photoelectric effect is more likely below 57 keV. Above 57 keV Compton scattering becomes dominant interaction in silicon.

The deposited energy creates electron-hole pairs in the sensor. If we assume that all the deposited energy is contained in the sensor volume the number of created electron-hole pairs depends on the deposited energy and the average energy required to create electron-hole pairs. The average energy required to create a electron-hole pair is the energy required to move an electron from the valence band to the conduction band (which leaves a hole in the valence band). The average energy depends on the sensor material. The electron-hole creation energy is higher than the band gap of the semiconductor as energy is lost in other processes in the semiconductor.

Free charge carriers are collected with electrodes by applying an electric field across the material. This electric field makes the free charge carriers move towards the collection electrodes. The collection electrodes are on the front and backside of the semiconductor. The backside of the semiconductor has pixelated electrodes and the front side, facing towards the incoming radiation, is a single electrode over the whole area of the sensor. The movement of these free charge carriers induces an electrical current. This current can be calculated using the Shockley-Ramo theorem.

The induced current created by the movement of the free charge carriers is captured using the readout electronics. The readout electronics typically have three

stages. In the first stage, the induced current is amplified using a charge sensitive amplifier. In the second stage, the amplified current is then processed by a pulse shaper. The pulse shaper is a band-pass filter and its intention is to increase the signal-to-noise ratio. In the last stage, the signal produced by the pulse shaper is compared to a user-determined threshold and the corresponding counter is increased. The counter value is temporarily stored in memory to be captured by ASIC readout electronics. There can be, and usually is, multiple thresholds so imaging with multiple thresholds simultaneously is possible.

3.1 Limitations

Next, I will discuss the limitations met in real photon counting detectors focusing mainly on the limitations of high-Z semiconductor sensors. This section relies heavily on [14].

3.1.1 Electronics limitations

As usual, the electronics have random noise which degrades the energy resolution of a pixel. The random noise in electronics can be specified using equivalent noise charge (ENC) which is defined in [14] as

$$\mathrm{ENC}^2 = (C_d + C_{\mathrm{in}})^2 \left[\frac{V_{\mathrm{thermal}}^2}{\tau_s} a_w + A_f 2\pi a_f \right] i_p^2 \tau_s a_p \tag{19}$$

where C_d is the detector capacitance, C_{in} is the capacitance at the input node, V_{thermal}^2 is the power spectral density of the thermal noise of the input transistor, τ_s is the shaping time in the shaper circuitry, A_f is the flicker noise of the transistor, i_p^2 is the power spectral density of the parallel noise source, a_w,a_f and a_p are constants related to the shaper transfer function. In this case, the ENC is defined as the ratio of the total root mean square noise at the output of the pulse shaper to the signal amplitude due to one electron input charge [14]. The capacitance in the MOSFET input gate is included in the C_{in} capacitance. From here it can be seen that the ENC isn't proportional to the energy of the incoming photons. This means that the impact of the ENC in energy resolution is constant regardless of the energy of the incoming photons.

Another limitation of the electronics side is pile-up. The pile-up happens because

x-ray photon events in the semiconductor sensor happen so often that the signal processing chain can't keep up with the number of events per second. This means that in the signal processing chain consecutive photons overlap at high flux rates which hinders the ability to discern photons in time. This results in a loss of counts and distortion in the pulse amplitude measurement done by digitization after the shaper in the signal processing chain.

The arrival of consecutive photons is due to the Poisson distributed random process of the x-ray photon events in the semiconductor sensor. This means that the probability density function of time between successive pulses is the same as the probability density function of the Poisson process or exponential law

$$p(t) = r \exp(-rt) \tag{20}$$

where r is the average incoming photon rate and t is time. [14]

This leads to two main types of pile-ups namely peak pile-up and tail pile-up. In peak pile-up, the arrival times coincides so that the second pulse increases the amplitude of the first pulse which results in a single count for two pulses. This single count has a higher amplitude than the first pulse. In the tail pile-up, the tail of the first pulse is distorted by the second pulse. The second pulse increases the tail of the first photon but the second pulse isn't counted as the shaper output is still decreasing from the first photon event.

Depending on the functionality of the pulse processing chain pile-up can be dealt with in multiple ways. According to [14] two common ways are paralyzable and non-paralyzable processing chains. In the paralyzable chain, an event happening during the dead time from photon events aren't counted and the dead time is increased by another dead time for every event happening during the dead time, hence the processing chain paralyzes if multiple events are happening during the dead time as this extends the dead time by another dead time multiplied with the number of events happening during the dead time. Non-paralyzable processing chains ignore photon events happening during the dead time which means that the events don't affect the measurement.

Other limitations are for example due to the manufacturing process of the pixel and the electronics in the CMOS process. The manufacturing defects can lead to uneven pixels or even dead pixels. In the case of uneven pixels, the threshold

values have to be calibrated in order to guarantee the homogeneity of the sensor. Practically perfect calibration isn't possible thus non-homogeneity of pixels can lead to a reduction in energy resolution. In particular, this can be a problem when a photon counting camera is manufactured from multiple sensor chips laid side by side.

3.1.2 Semiconductor sensor limitations

The semiconductor sensor has its own limitations. In this section I will be going over absorption efficiency, partial charge deposition due to fluorescence and Compton scattering, statistical noise and Fano factor, charge diffusion and charge trapping, and sensor polarization.

The absorption efficiency depends on the proton number or density of the semiconductor material. The x-ray energy window of interest for this thesis is 20 keV to 150 keV which means that higher-Z materials are used as their quantum efficiency is high in this window. Germanium (Ge), Gallium-Arsenide (GaAs), Cadmium-Telluride (CdTe), Cadmium-Zinc-Telluride (CdZnTe) are common materials that obtain high quantum efficiency in the energy window of interest. Silicon is, for example, low-Z semiconductor material commonly used for semiconductor detectors and it has many positives like homogeneity, cost and availability however thin layers of silicon have rapidly decreasing quantum efficiency for energies over 20 keV. This means that silicon becomes non-ideal material for the energy window of interest however it can be used for biomedical imaging applications where the energy window is in the range with more optimal quantum efficiency. Edge-on silicon detectors have been developed [15], [16].

As mentioned earlier the two dominant x-ray interactions with material are the photoelectic effect and Compton scattering. Both of these interactions can lead to a partial charge deposition which can distort the measured energy spectrum.

For CdTe sensor the dominant interaction is the photoelectric effect in which a characteristic fluorescence photon can be emitted. If this characteristic fluorescence photon is emitted it carries away some part of incoming energy which means that the detected energy is significantly less. The K-edges are at the energy of 26.711 keV and 31.814 keV for Cadmium and Telluride respectively. The energies of the photons generated from these K-alpha fluorescence photons are 23.17 keV for K_{α_1} and 22.984 keV for K_{α_2} in Cadmium and for the Telluride they are 27.44 keV for K_{α_1} and 27.202 keV for K_{α_2}. The yields for fluorescence photons are 83.6 % for Cadmium and

Element	Z	K-Edge (KeV)	Yield	$K_{\alpha 1}$ (KeV)	$K_{\alpha 2}$ (KeV)	$d_{\alpha 1}$ (µm)	$d_{\alpha 2}$ (µm)
Si	14	1.839	0.050	1.73998	1.73938	11.86	11.86
Cd	48	26.71	0.843	23.1736	22.9841	113.2	110.7
Te	52	31.81	0.877	27.4723	27.2017	59.32	57.86
Ga	31	10.37	0.507	9.25174	9.22482	40.62	40.28
Ge	32	11.10	0.535	9.88642	9.85532	50.85	50.4
As	33	11.87	0.562	10.54372	10.50799	15.62	15.47

Table 1. K-edges and fluorescence photons for common semiconductor materials for x-ray sensors. Data: K-edges: [1], Yields: [17], Transition energies: [18]

for Telluride it is 87.3 %. So it is very likely that in the usual x-ray window 1 keV to 150 keV fluorescence photons are emitted in the CdTe-sensor. It is possible for the fluorescence photons travel to another pixel as the mean free path for K_{α_1} photon is 113 µm and for K_{α_2} it is 110.7 µm in Cadmium. Respectively for Telluride the mean free paths are 59.32 µm and 57.85 µm. This means that it is likely for photons to travel neighbouring pixels for the typical pixel sizes range 50 µm to 120 µm. For other common sensor materials the photoelectric edges and the properties of fluorescence photons are in table 1

In compton scattering the partial charge deposition happens due to energy and momentum transfer from the photon to an electron. The photon scatters from its initial trajectory and the electron gets emited at an angle. There is a maximum for the kinectic energy of the electron and it happens when the photon is fully backscattered. This maximum energy transfer is known as the Compton edge.

Statistical noise in the semiconductor detector can be thought of as the minimal noise or limiting resolution R that would be in the detector no matter how perfect the detector is. This statistical noise or fluctuation is due to the charge carriers generated in the detector being a discrete number instead of being a continuous variable. The number of charge carriers generated fluctuates even though the energy deposited to the semiconductor detector remains the same. This fluctuation can be estimated by assuming the formation of a charge carrier being a Poisson process. However, measurements have shown that the formation of individual charge carriers is not independent and thus can't be fully modelled by simple Poisson statistics. Fano factor has been introduced to quantify the difference between observed statistical fluctuations and the statistical fluctuations estimated using pure Poisson statistics. [6]

The pure Poisson statistics assumption gives

$$R = \frac{2.35}{\sqrt{N}} \tag{21}$$

for the limiting resolution R as a function of the number of the charge carriers N. The Fano factor equivalent for limiting resolution is defined as

$$R = 2.35\sqrt{\frac{F}{N}} \tag{22}$$

where F is the Fano factor. Fano factor is determined by comparing measurements of limiting resolution with limiting resolution given by Poisson statistics. Fano factor can be also represented in terms of Full-Width at Half-Maximum (FWHM) as

$$\frac{\text{FWHM}}{E_0} = 2.35\sqrt{\frac{F}{N}} \tag{23}$$

where E_0 is the absorbed energy. This representation is useful as energy sensitivity is typically measured as FWHM of known monochromatic x-ray source.

Charge diffusion happens in the semiconductor sensor when the free charge carriers produced by x-ray photon interactions are drifting towards the electrodes. During this drift, the charge cloud spreads out due to diffusion and electromagnetic repulsion. This can result in charge sharing between adjecent pixels when the photon interacts close to the edges of adjacent pixels. This charge sharing results in a low energy tail in the energy spectrum. This tail results in increased counts at the observed low energy spectrum. Charge sharing impact increases as the ratio between pixel pitch and sensor thickness decreases. Charge sharing can be reduced by increasing the bias in the sensor as this shortens the drift times.

Because semiconductors have defects the charge carriers can become temporarily trapped in the medium. This means that the signal in the readout is reduced as the trapped charge carriers can't reach the readout electronics. Charge trapping is more pronounced in high-Z semiconductor sensors, due to impurities in the semiconductor process. Charge trapping can be reduced by making the sensor thinner, increasing the bias or using materials with higher carrier mobility. [19].

The trapping and de-trapping inside of the semiconductor sensor can lead to the sensor being polarized which reduces the count-rate and charge collection efficiency of the sensor. This trapping and de-trapping affect the electric field profile in the

semiconductor sensor. Polarization can be minimized using higher bias voltage and low operation temperature.

3.2 Medipix family and Medipix 3RX

The first chip in the Medipix family was a readout chip for a 64×64 pixel matrix with a pixel pitch of 170 µm. It was developed as a part of the Medipix project based on the design of the LHC1/Omega3[20] chip but tuned specifically for imaging applications. [21] The modifications includes modified pixel shape from a narrow rectangle to a square and a counter for each pixel. First Medipix was released in 1997 and currently Medipix chips are licensed by the detector manufacturers so multiple manufacturers are creating the chips based on the licensing agreement. [22]

Medipix 2 had multiple iterations until the final version MPIX2MXRV2 released in 2005 [22]. The final version of Medipix 2 featured 256×256 square pixels on a pitch of 55 µm. In the design of Medipix 2, the dead area was minimized on 3 sides to make it possible to connect multiple chips to make a single camera. This minimization was done by introducing periphery on the fourth side which was used to minimize the nonsensitive area for the other three edges to less than 50 µm. This reduction resulted in detection area of 1.98 cm^2 which means that 87 % of the entire chip area is sensitive. [23]

Because pixel size was reduced from 170 µm to 55 µm the charge sharing effect became more pronounced as the distance between pixels became shorter.

For Medipix 2 the CMOS process was changed from 1 µm to 250 nm. This change made the individual transistors smaller which allowed reduction of pixel size together with an increased number of metal interconnect layers [24]. Some new features were also implemented namely per pixel leakage current compensation, selectable charge carrier sensitivity to either holes or electrons and an energy windowed discriminator. The preamplifier was changed from the design of LHC1's folded cascade circuit to a Krummenacher preamplifier proposed by F. Krummenacher in [25].

The final version of Medipix 3RX was released in 2013 [26] [14]. Albeit the CMOS process was changed from 250 nm to 130 nm the pixel size and number of pixels remained the same as in Medipix 2. The most notable improvement was the charge summing mode. This was introduced to combat the charge sharing effect, especially with higher-Z materials. Charge sharing, especially with the smaller pixel size, worsens the spectroscopic capabilities of the detector.

In the charge summing mode, the signal is reconstructed in each pixel from the neighbouring pixels by summing the charge recieved by the pixel and its neighbouring pixels. After this, the reconstructed signals are compared and the pixel with the highest reconstructed charge is counted as the hit pixel. The reconstructed signal must be stronger than a programmed energy threshold value. If the reconstructed signal is weaker than the programmed energy threshold it is ignored.

Medipix 3RX can be made with larger pixel size by combining four 55 µm × 55 µm pixels to a single 110 µm × 110 µm pixel. This reduces the effect of the charge sharing and enables usage of 8 thresholds at maximum in SPM mode.

Medipix4 is under development as of writing this thesis. At the moment of writing this thesis, an article on the new analog front-end Medipix4 has been released [27]. Compared to Medipix 3RX the pixel size has been increased from 55 µm to 70 µm to better accomamodate free paths of the high-Z sensor materials which reduce the amount of charge sharing happening between pixels of the sensor. Once again it is possible to combine the four 70 µm pixels into a one 140 µm pixel.

Medipix4 is intended to be tiled from all four sides which mean that Y by X sensors should be possible. This however means that there won't be space for peripheral logic or through-silicon vias input/output (TSV IO) pads as the input pads extend on all the edges of the chip. This requires the usage of redistribution lines (RDL) which have the intent of equalizing the capacitance between the sensor pad and the readout pixel. These redistribution lines are placed on the top layer of the Medipix4. The addition of the redistribution lines means the front-end input capacitance will be increased which then leads to an increase in the equivalent noise charge.

Medipix 3RX consists of two parts: the semiconductor sensor and the reading electronics. Let's focus on the reading electronics first.Analog circuitry consists of the Krummenacher preamplifier, mentioned earlier, and the discriminators. The analog circuitry can be seen in figure 4. Details on the Krummenacher preamplifier can be read from [25] as the description of the Krummenacher preamplifier is out of the scope of this work. However, it should be noted that the Krummenacher preamplifier and shaper exposes internal current values which can be modified by the user.

The Krummenacher preamplifier is paired with a capacitor via feedback. The value of the feedback capacitor determines (partially) the gain of the Medipix 3RX

chip and the value can be chosen from values 7 fF, 14 fF, 21 fF and 28 fF. This means that Medipix 3RX chip has four selectable gain modes from the highest gain mode with feedback capacitor value of 7 fF) to the lowest gain mode with feedback capacitor value of 28 fF. The gain modes are named super high gain mode, high gain mode, low gain mode and super low gain mode, respectively to the capacitor values listed earlier.

The next part of the Medipix 3RX circuitry is the shaper which is a first-order semi-gaussian shaper that has a time constant of ≈120 ns.

The shaper is then connected to one discriminator that compares the signal level to two thresholds set by the user. The shaper has three other current lines connected to neighbouring pixels. This is another point that allows end-user control as the Medipix 3RX can be operated either in single-pixel mode or charge summing mode. In the case of the single-pixel mode, the charge received by the pixel is compared to the threshold value *Threshold_0* in *Discriminator threshold 0* shown in figure 4. If the incoming charge from the pixel is higher the than value set in *Threshold_0* the pixel counter is increased.

Single-pixel mode can be used either in one channel or two-channel mode as there are two counters per pixel. In two-channel mode, the incoming charge is compared by the *threshold discriminator 0* and *threshold discriminator 1* in figure 4 depending on if the charge is higher than either of the thresholds corresponding counter is increased. In single-pixel mode on summing circuit connected to the *threshold discriminator 1* the currents incoming from neighbouring pixels are ignored and the current incoming from the pixel at hand is fed directly to the *Discriminator threshold 1* in two-channel mode. Single-channel mode ignores *Discriminator threshold 1* entirely.

In the charge summing mode *threshold discriminator 0* has to be passed by the charge to be considered as an x-ray incoming to the pixel. The pixel counter is incremented in the case that the total summed signal passes threshold *Threshold_1*. However, the pixel whose counter is incremented is determined from the partial signals of the neighbouring pixels in arbitration logic which resides in the digital logic shown in figure 4. The arbitration logic picks the pixel with the highest partial charge signal to have its counter incremented.

The counters in pixels are linear feedback shift registers which can be configured either as 2 × 1-bit counters, 2 × 6-bit counters, 2 × 12-bit counters or combined as 1 × 24-bit counter. These counters can be either read either sequentially or

continuously. In the continuous operation mode, there won't be deadtime however only one counter can be used as the other one will be written when the other one is read. The threshold for reading the counter can be adjusted by the user.

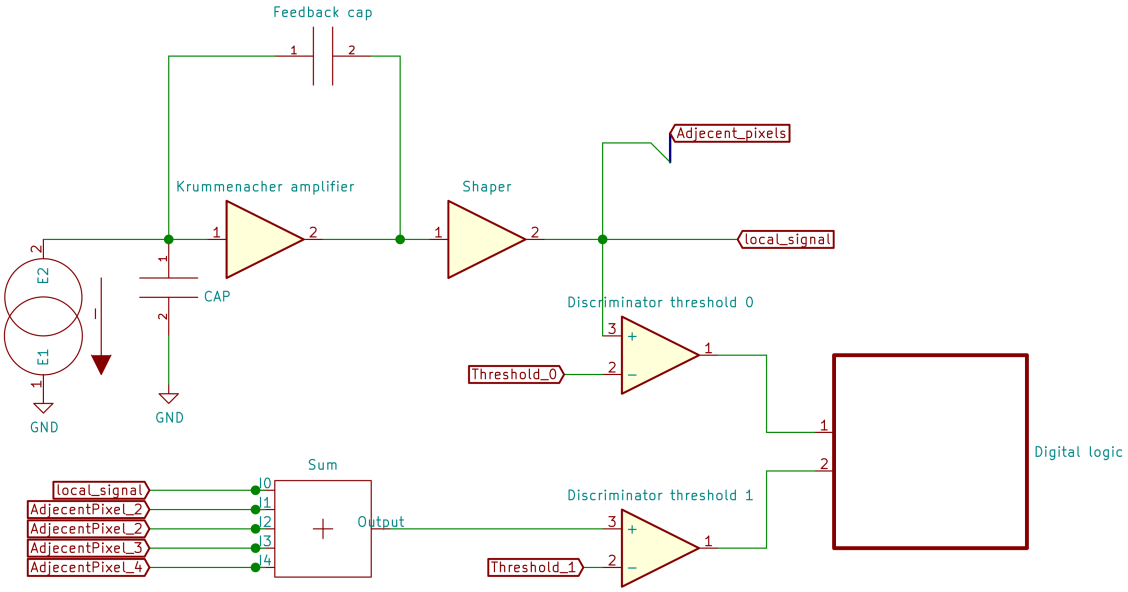

Figure 4. Analog side of the Medipix 3RX, 2021, Data: [26]

3.3 Advacam

The camera used in this thesis was manufactured by Advacam. The configuration of the camera was 2×5 panels meaning that two cameras with 5 panels were combined as one camera. Both cameras can be operated separately if needed. The sensor is CdTe sensor with pixel size of 55 µm. The manufacturer specifies the spatial resolution to be 9 lp/mm and the energy resolution to be 1.2 keV to 3.6 keV for CdTe sensor. The energy resolution is given as standard deviation σ which relates to full-width at half maximum by

$$\mathrm{FWHM} = 2\sqrt{2\ln 2}\sigma \tag{24}$$

which is used in this thesis. Minimium detectable energy for CdTe sensor is specified to be 5 keV.

4 Measurements

The properties chosen to be characterized were noise edge, photon couting speed, energy resolution and spatial resolution. The noise edge means the lowest energy threshold before hitting the noise floor in energy level.

The photon counting speed is the maximal photon flux which the camera can count without having pile-up from the camera. However, there might be pile-up regardless of how low the photon flux is. This is due to the nature of the timing between photons.

Energy resolution is one of the most important properties of the photon counting detector as the idea is to be able to do x-ray imaging with certain energy threshold(s). The energy resolution was characterized by measuring the spectrum of the x-ray tube and Americium-241 isotope. Another way used to determine the energy resolution was mass attenuation coefficients measurements. These mass attenuation coefficient measurements were done using two Gold foils, Niobium and Rhodium. From mass attenuation coefficient measurement, it is possible to determine the full-width-half-maximum of the energy resolution by fitting erf-function to the increase in mass attenuation coefficient from K-edges.

Spatial resolution is an important property of the x-ray camera along the energy resolution as the spatial resolution determines smallest features that can be detected in the images. The typical ways to determine the spatial resolution are using resolution targets or determination of modulation transfer function. The modulation transfer function was chosen as this way only requires a target with a sharp edge. The target for modulation transfer function measurement was more readily available and thus this method was chosen for this thesis to determine the spatial resolution.

The x-ray tube used in these measurements were Hamamatsu L12161-07, with tube voltage from 40 kV to 150 kV and maximum output of 75 W. This x-ray tube was at fixed lenght of 420 mm from the x-ray camera.

4.1 Noise edge measurement

Noise edge measurement was performed to estimate the lowest usable threshold for the threshold 0. This was an important measurement as the result is used to determine lowest possible energy threshold for threshold 0 in charge summing mode. This noise edge threshold also determines the lowest usable threshold for measurements in charge summing mode as the actual threshold, threshold 1, has to be higher than the threshold 0.

The measurement was quite a simple threshold scan of threshold 0 without any x-rays. This measurement was done for both narrow and super narrow gain modes in the Advacam camera. The wide gain mode was skipped as it is very unlikely to be used in future measurements.

The measured mean counts per panel are presented in figures 5a and 5b in narrow gain mode for halves D02-W0558-5 and G04-W0558-5 respectively. For the rest of this thesis I will be refering half D02-W0558-5 and G04-W0558-5 as halves D02 and G04 respectively. The results for super narrow gain mode are presented in figures 6a and 6b. From these results, it was determined that the threshold 0 should be higher than 8 keV. This was chosen as the value as it appears to have safety margin for noise floor and rest of the measurements has higher lowest energy threshold than 8 keV so safety margin optimization was not necessary.

From the figures 5a and 5b, it can be seen that the DO2 and G04 halves are pretty even in terms of the noise edge in the narrow gain mode. However the G04 seems slightly noisier at the 4 keV to 6 keV energy range. The super narrow gain mode is more even between the two halves and has slightly lower noise edge as seen in figures 6a and 6b. This should be taken in consideration when measurements are done at lower energies. For the measurements done in this thesis, using 8 keV as the threshold 0 seems to be safe and has safety margin.

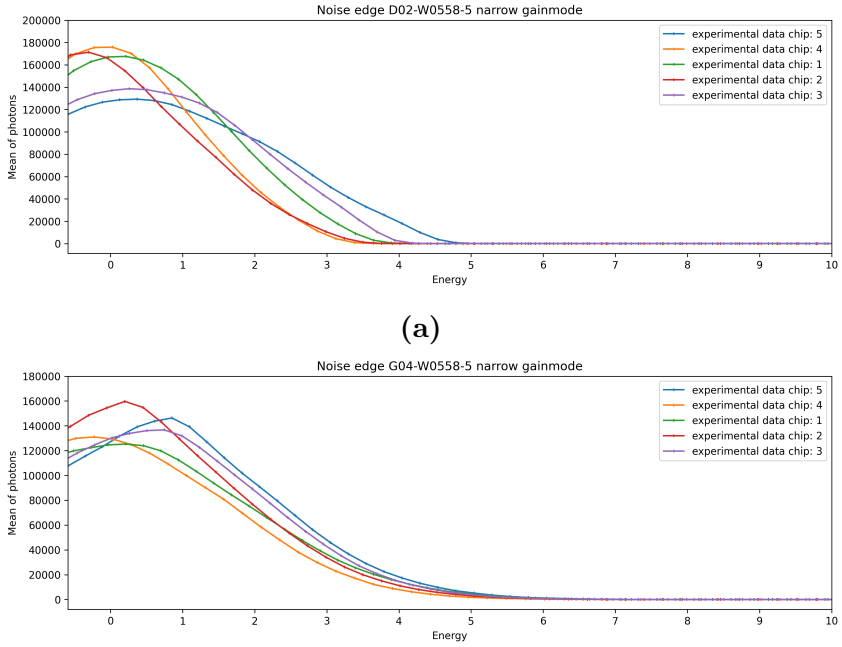

(a)

(b)

Figure 5. The noise edge of the D02 (a) and G04 (b) side in narrow gain mode.

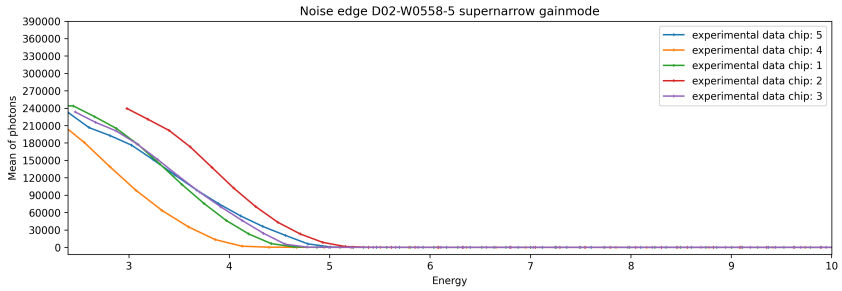

(a)

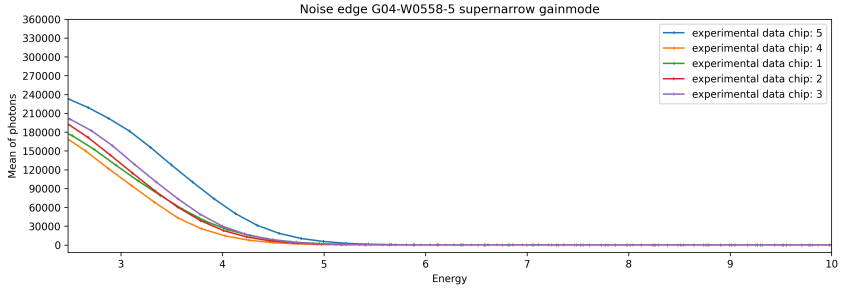

(b)

Figure 6. The noise edge of the D02 (a) and G04 (b) side in super narrow gain mode.

4.2 Photon counting speed

The photon counting speed of the camera was determined in order to make sure that pile-up will not affect measurements. This was determined by assuming that at a low tube current every x-ray is captured. I assumed that the number of x-rays captured is linear up until pile-up begins to happen. There isn't a way to know if the assumption that at low the x-ray tube current all photons are captured is true. Also due to randomness in time differences in photons entering the sensor, there can be pile-up at low photon fluxes.

This measurement was done using both single pixel mode and charge summing mode with threshold 0 set to 10 keV in single pixel mode. In charge summing mode, the threshold 0 was set to 8 keV and threshold 1 was set to 10 keV in accordance to single pixel mode. Images were captured using 50 s exposure time.

The x-ray tube was set to 150 kV with HE-1[1] filter and the current was scanned from 10 µA to 400 µA with step of 5 µA. After each current step the x-ray tube was let to stabilize for 50 seconds before taking the next picture.

The pictures were processed by taking the sum of all pixels per panel for each current value. The current values were then converted to units of $\frac{1}{\text{pxs}}$ with assumption that at low x-ray tube current the amount of counted photons would be same as the number of photons coming from the x-ray tube. This assumption can be formulated as

$$\frac{N}{I} = \frac{N_0}{I_0}, \tag{25}$$

where N is the number of photons, I is the current value, N_0 is the number of photons at low current I_0. The I_0 was 10 µA. The measured values $\frac{N_{counted}}{N_{out}}$ are presented in figure 7 as a function of tube current. The values are means per half of the camera with standard deviation plotted under the line.

[1]The filter is made out of glass and has thickness of 1.1 mm.

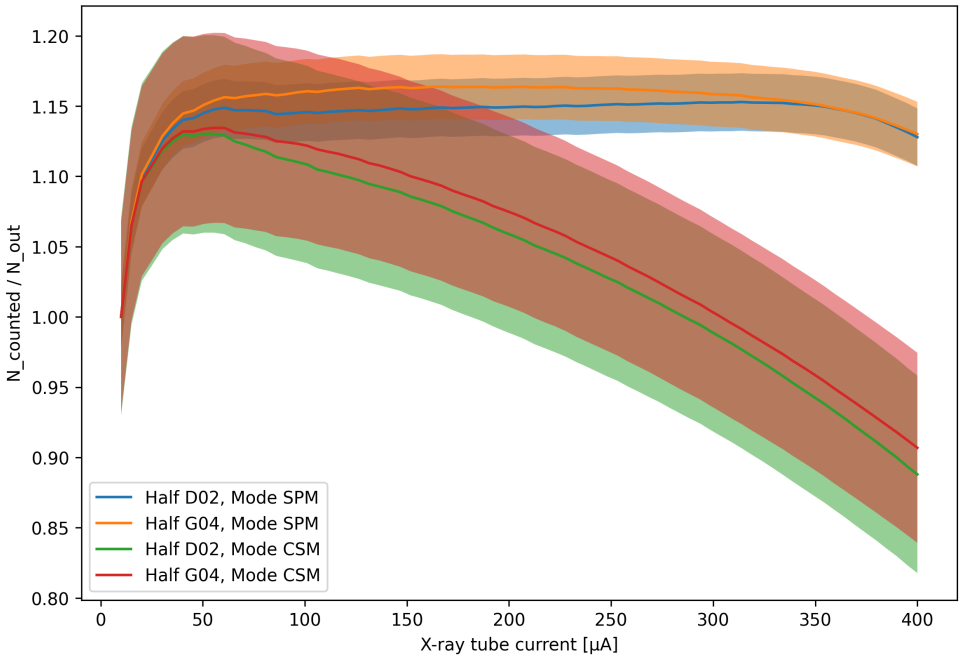

Figure 7. Average photon counts normalized by approximated number of photons outgoing from x-ray tube as a function of x-ray tube current. The standard deviation of panels per half is plotted as a shaded area under the average curves.

The assumption that all the photons at the low x-ray tube are being counted seems to be somewhat false as seen in the figure 7. The figure 7 shows that higherh tube current results in more counts being detected than what is expected based on the equation (25), particularly in SPM mode. It remains unknown whetever this discrepancy is solely due the camera or the x-ray tube or does both have some effect in this discrepancy.

One the causes for the discrepancy in the x-ray tube side could be that the number of photons produced in the x-ray tube doesn't scale linearly at lower tube currents, but after some current value the number of photons begins to scale linearly. This could be the case as the ratio $\frac{N_{counted}}{N_{out}}$ remains roughly 1.15 in the current range 100 µA to 350 µA. Another possibility is that the tube isn't quite stabilized at the beginning of measurement sets but stabilizes after a while during the measurement.

In the camera, one factor leading to the discrepancy could be the internal flourescence photons from the CdTe sensor which would mean that the number of counted photons is slightly higher than the number of photons incoming as some

fluorescence photons are created inside the sensor. Another factor is the diffusion of the charge cloud which results in counts in neighbouring pixels from a single photon.

The behaviour on charge summing mode seems to be correct as it is possible that the charge summing mode can't keep up with the photon flux even at lower tube currents.

Based on this measurement alone it is hard to determine what is the cause of this discrepancy and more measurements would be necessary. With this kind of a measurement setup, there isn't a way to count or determine the true number of incoming photons from the x-ray tube.

4.3 Threshold scan of the x-ray tube

Threshold scan of the x-ray tube was chosen as one of the measurements to roughly characterize the energy resolution and to determine if it would be possible to see the characteristic K_α x-rays from the tungsten target of the x-ray tube. The measurement was done using the charge summing mode with threshold 0 set to 8 keV and the threshold 1 was scanned from 43 to 195 DAC units with a step size of 1. This translates, roughly, to an energy range of 16 keV to 107 keV with a step size of 0.550 keV as the threshold scans are done using the DAC values. The measured energy range differs per panel. This discrepancy is due to the calibration of the DAC values to energy which differs per panel. To maximize statistics, 160 images were taken on each threshold 1 value each with 0.25 s of exposure time.

The tube settings were chosen so that the spectrum emitted by the x-ray tube would be optimal for capturing the characteristic K_α x-rays. The tube voltage was set to 150 kV with a tube current of 100 µA and a HE-6[2] filter was used to cut the lower end of the energy spectrum.

The images were then processed to construct an energy spectrum from the photon counts measured on each threshold 1 step. The processing began by choosing a region of interest for each panel. This region of interest was chosen so that the bad pixels in the corners of each panel were ignored. The region is roughly 128×128 pixels from the center of the panel. From this region interest, pixels were randomly chosen and their counts were plotted as a fuction of threshold 1. The per-pixel counts were then differentiated using local fitting. In local fitting, I chose some region covering the measured energy threshold and fitted a polynomial to the range of measured

[2]The filter is made out of glass and has thickness of 5.0 mm

values in the region. The region included points under and above the chosen energy threshold for each measurement. The differentation was evaluated at the chosen energy threshold for each measurement. The differentation of the counts results in the count spectrum as the function of threshold 1. The plot can be seen in figure 8.

The expected result from the threshold scan of the x-ray tube would have been that the characteristic x-rays of the tungsten target would be somewhat visible in the spectrum in figure 8. However, due to the configuration of this camera, thick CdTe sensor with small pixel size, it was asummable that the characteristic x-rays wouldn't be visible. From the figure 8, it is very clear that the characteristic x-rays aren't visible at all and the spectrum contains mostlty Bremsstrahlung of the x-ray tube. From the figure 8, there appears to be some discrepancy between the spectrum position between pixels. This effect is more pronounced on the Americium-241 measurement. Similiarly to [28] the CSM spectrum matches with the spectrum measured in SPM mode with higher pixel pitch of 110 µm.

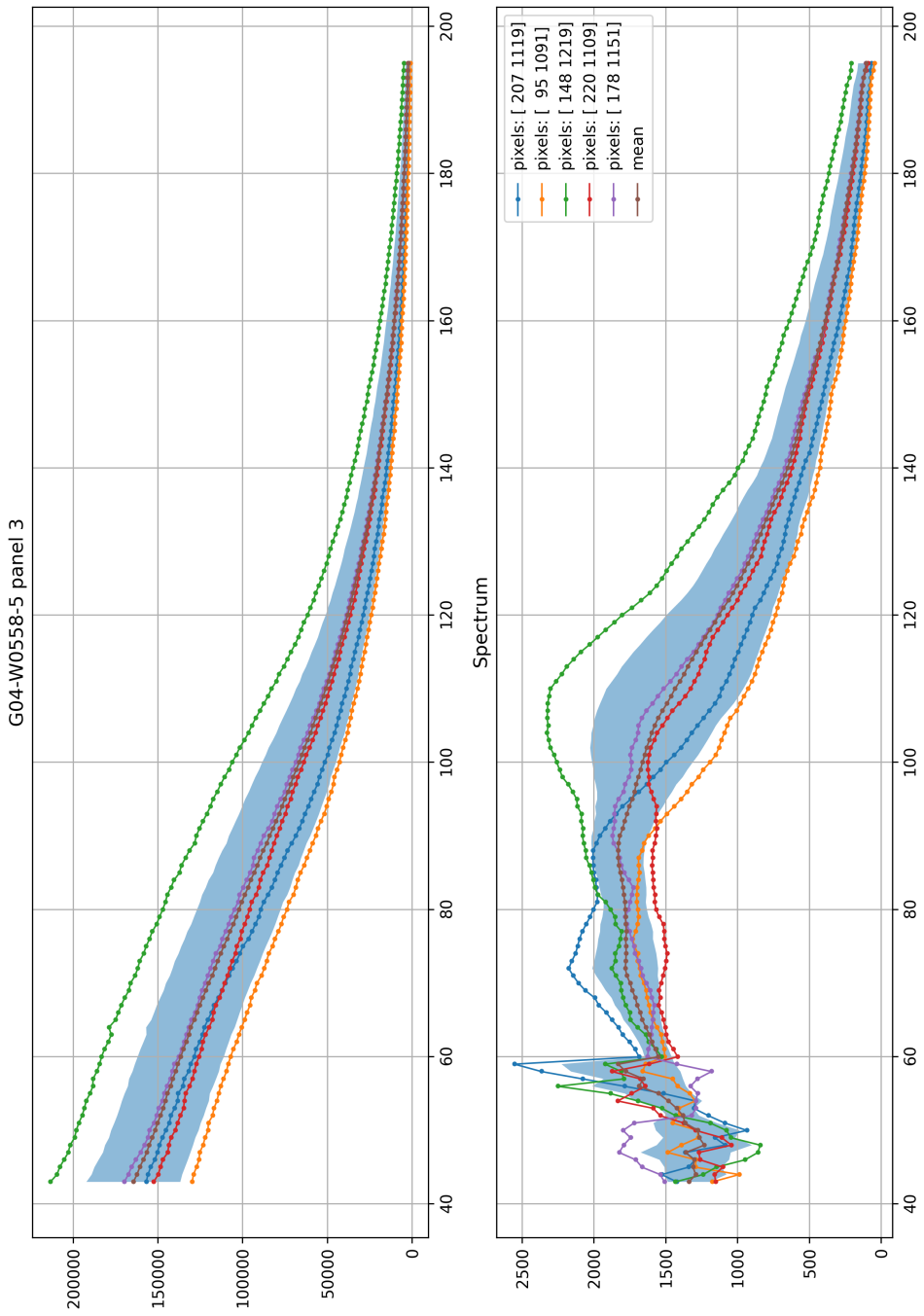

Figure 8. Spectrum of the x-ray tube plotted from 5 randomly selected pixels. The mean from the 5 random selected pixels and it is standard deviation is plotted in lighter blue.

4.4 Americium-241 measurements

Americium-241 radiation source was chosen for determination of the energy resolution. The Americium-241 has intensive characteristic x-rays at the energy of 59.5409 keV and at 26.3446 keV [29]. The measurement was attempted with lower activity radiation source (JYFL-033) however the measurement was inconclusive and the measurement was repeated with higher activity radiation source (JYFL-76). The lower activity source had activity of 384.50 kBq in 1970 and the higher activity source had activity of 3.7 GBq in 2006.

At first, the measurement was done without an aluminium filter plate as seen in image 9. However it was determined that unwanted low energy characteristic x-rays from the Am-241 source and from the CdTe sensor itself were a problem in the measurement. The aluminium filter plate was used to attenuate these low energy characteristic x-rays. The collimator in the radiation source allowed imaging with only one panel, thus only panel 3 of D02 half was analyzed.

The placement of the aluminium plates can be seen in figure 10. The plates were 2 cm apart from the camera and from the source. The source was 4 cm away from the camera.

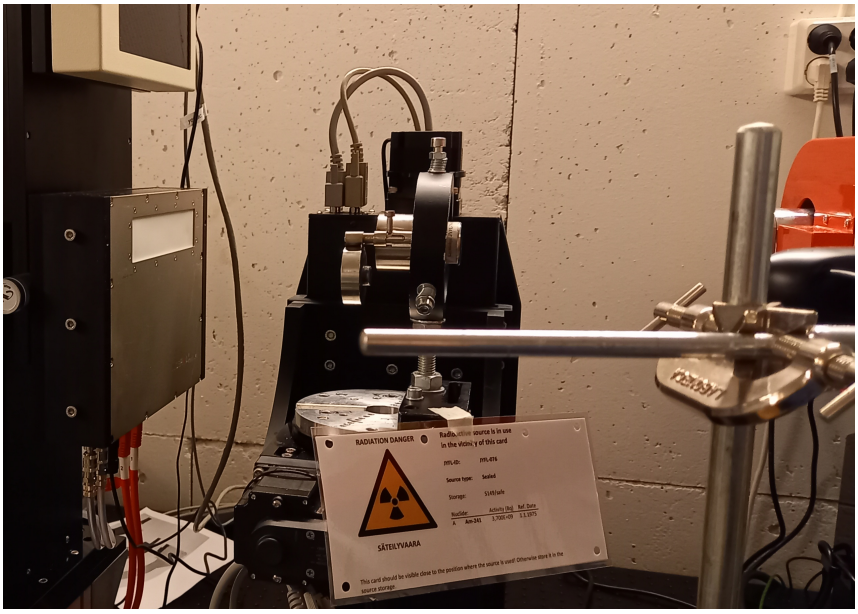

Figure 9. Initial measurement setup for the Americium-241 radioisotope. The camera is on the left, in the middle is the source inside of a collimator with collimator in open position. The radiation source was fixed using optical mounting mechanism to the sample table of the JTOMO-setup.

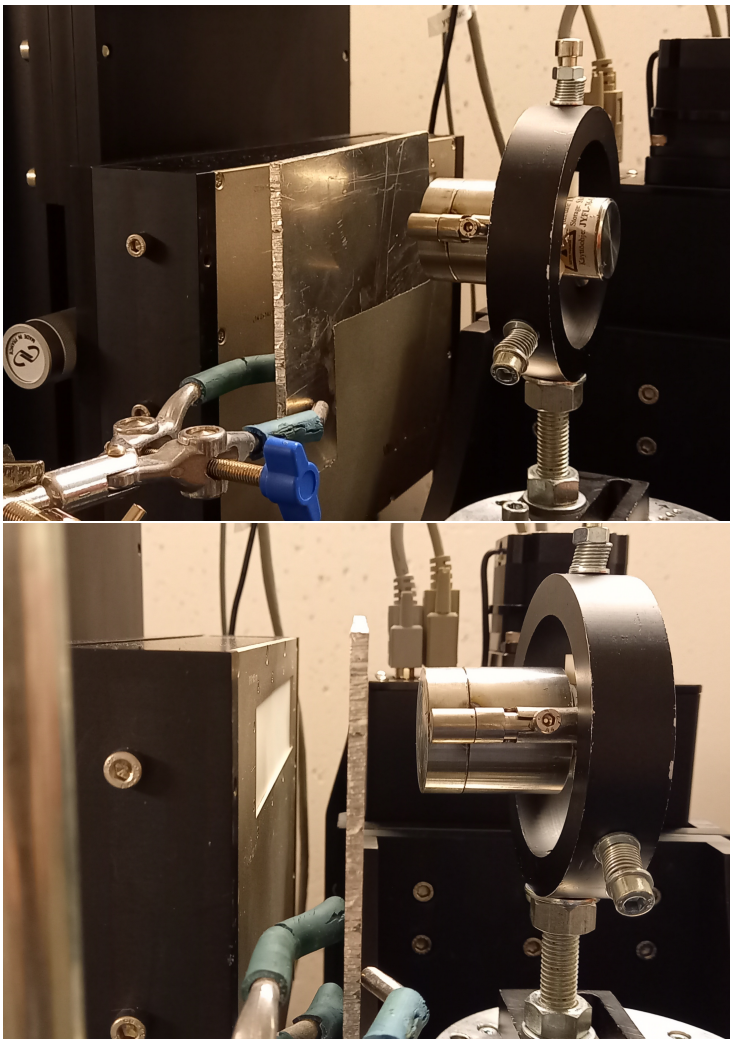

Figure 10. The same setup as in the figure 9 but with 4 mm aluminium plate fixed between the radiation source and the camera.

The settings for the camera was exposure time of 200 s per threshold value. The CSM mode was used with threshold 1 being scanned from 27 to 99. The threshold 0 was 7.9915 keV for panel 3 of DO2 half.

In figure 11, the photon counts were plotted as a function of DAC values and the spectrum similarly as in the x-ray tube threshold scan. However, there is a DAC value shift between pixels which can be seen from the results in figure 11. I attempted to fix the shift by assuming that last spike is caused by the 59.5409 keV characteristic x-ray in question and moving highest spikes to zero. The shift fixed spectrum can be seen in figure 12.

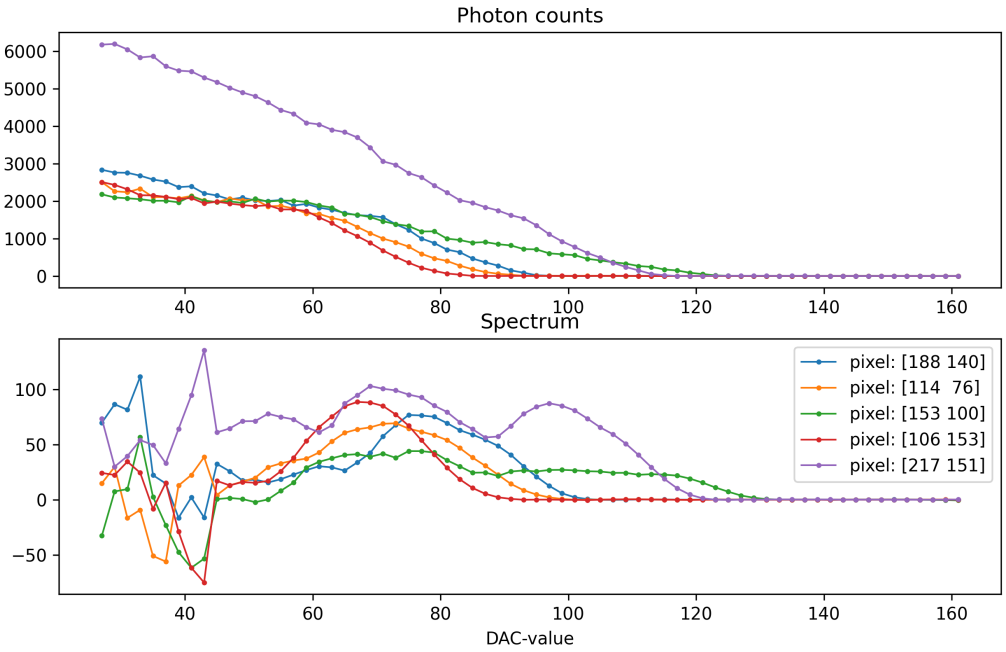

Figure 11. The Americium-241 spectrum from 5 randomly chosen pixels near the centre of the panel 3 in D02 half. Note that the spectrum is very different from pixel to pixel and the 59.5409 keV characteristic x-ray from the radioisotope isn't visible.

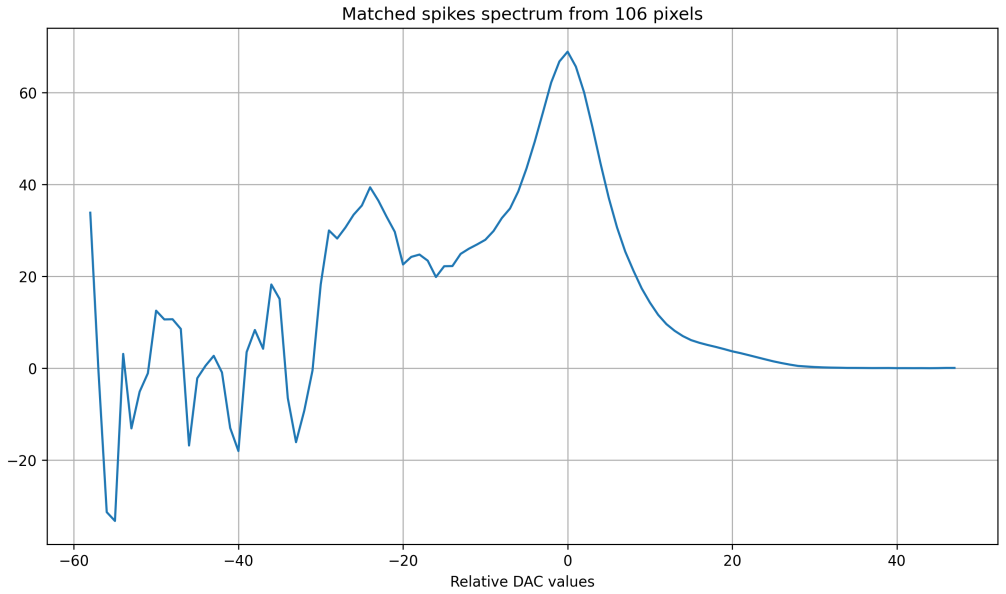

Figure 12. Americium-241 spectrum sampled from 106 pixels with the assumed 59.5409 keV moved to relative DAC value of 0. Fitting Gaussian function to the spike gives Full-Width-Half-Maximum of 8.54 ± 0.10 in DAC units.

Clear result from the Americium-241 measurement is that at least on the charge summing mode there is discrepancy between the pixels in the DAC-values. After naive matching of the spikes from the assumed 59.5409 keV characteristic x-rays, it can be seen that the full-width-half-maximum is 8.54 ± 0.10 DAC-values obtained by Gaussian fit. This FWHM translates to roughly 10.00 ± 0.11 keV as 1 DAC-value corresponds to roughly 1.1 keV in the calibration data of the camera. This is roughly the same full-width-half-maximum as measured in the later gold foil measurements. However, the naive matching of the spikes isn't enough to actually determine the full-width-half-maximum from Americium-241 source. This could be possible if calibration is done and confirmed using other radioisotopes or monochromatic x-ray sources. It remains unknown how the current calibration behaves with different x-ray energies. The pixel-per-pixel differences might be different when different x-ray energies are used.

4.5 Gold foil measurements

To further gauge the energy resolution, I measured the transmittance of 5 µm and 490 µm thick gold foil samples.

The measurement was done by scanning threshold 1 in charge summing mode. Compared to the x-ray tube spectrum scan, this measurement requires two images: one with and without the target foil between the x-ray tube and the camera.

From transmittance, it is possible to determine mass attenuation coefficient. Mass attenuation coefficient can be calculated using equation (6) and rewriting the attenuation coefficient μ as a mass attenuation coefficient $\frac{\mu}{\rho}$ where ρ is the density of the object. However due to photon counting detector the intensities have to be changed to number counts N and N_0. This means that the units of $\frac{\mu}{\rho}$ is cm^2/g. The equation (6) then becomes

$$N = N_0 \exp\left(-x\left(\frac{\mu}{\rho}\right)\rho\right), \tag{26}$$

where x is the thickness of the homogenous material. The equation (26) can be then solved for $\frac{\mu}{\rho}$

$$\left(\frac{\mu}{\rho}\right) = \frac{1}{x\rho}\ln\left(\frac{N_0}{N}\right). \tag{27}$$

According to (11) the measured photon counts are integrals over the whole energy

range starting from E_{th0} and continuing to maximum energy of the spectrum of the x-ray source. The N_0 and N has to be differentiated in order to get the number of photons between the energy range $[E,E + \Delta E]$ where ΔE is the energy step size used in the measurement. Thus we get

$$\left(\frac{\mu}{\rho}\right) = \frac{1}{x\rho} \ln\left(\frac{\mathrm{d}N_0}{\mathrm{d}N}\right). \tag{28}$$

The measurement setup for thinner gold foil can be seen in figure 13. This setup was used for all foil measurements with varying dinstance between the camera and the foil. The distance between the camera and the foil was 28.5 cm for the thinner gold foil and 32 cm for the thicker gold foil. The distance between the foil and the camera was hard to measure due to long distance and danger of destroying the exposed CdTe sensor.

For both gold foils same settings in the camera and the x-ray tube were used except for scanned threshold range and filter used the in x-ray tube. The camera was set-up with CSM mode in narrow gain mode with 60 s exposure for all images. The DAC threshold 1 range used for thinner gold foil was 123 to 186 with step size of 1 threshold value which translates roughly to 50 keV to 110 keV with 0.6 keV step. The DAC threshold 1 range used for thicker gold foil was 81 to 176 with step size of 1 threshold value which is roughly 40 keV to 90 keV with 0.6 keV step. The threshold 0 was set to 8 keV for both foils. The x-ray tube was set up with voltage 150 kV and with current 100 µA. Only the filter was changed for each measurement such that for thinner gold foil HE-1 filter was used and for thicker gold foil HE-6 filter was used.

The measured transmittance values for thinner and thicker gold foils are in figures 14 and 15. As seen from the figures, the thinner foil passes almost all x-rays and the transmittance is noisier than the calculated transmittance of thicker gold foil.

The equation (27) can be used to calculate the mass attenuation coefficients from the transmittance. The mass attenuation coefficients are plotted in figures 16 and 17a.

From the mass attenuation coefficients, it is possible to determine the energy resolution by fitting erf-function and calculating the FWHM from the fit. This was possible only for the thicker gold foil as the mass attenuation coefficients for the thinner foil aren't increasing near the K-edge. The result from the fit was 10.1784 ± 0.0052 keV for FWHM from the thicker gold foil transmittance measure-

ment. The fit can be seen in figure 17b.

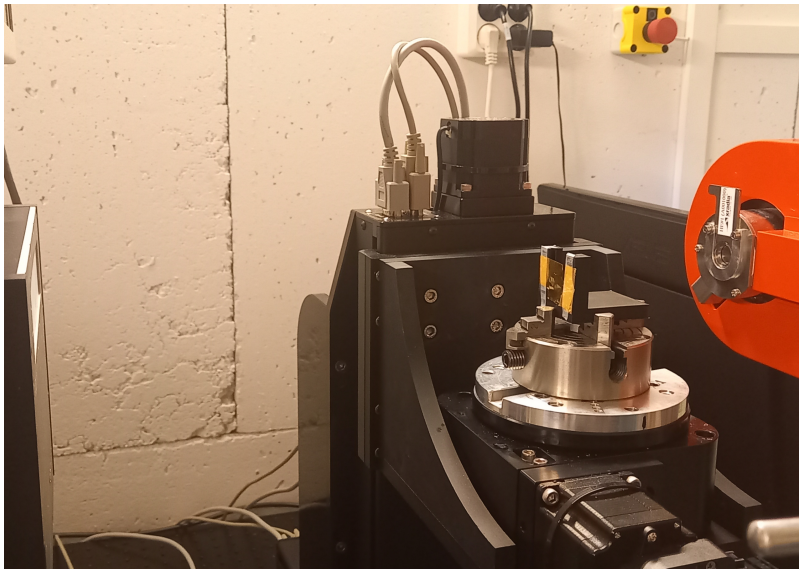

Figure 13. Measurement setup for all the foil measurements. The camera is on the left and the red x-ray tube is on the right. The sample is fixed on the sample table in the middle. The foil is fixed on 3D printed plastic support.

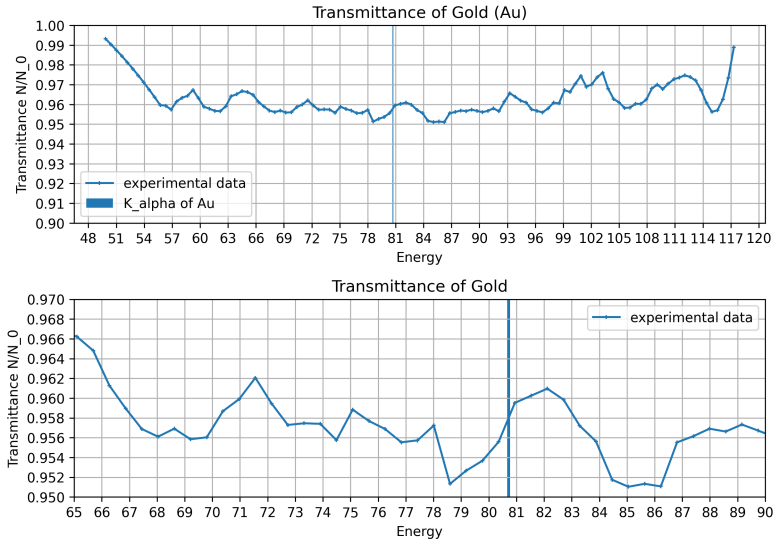

Figure 14. Transmittance of the 5 µm gold foil. From the graph it can be seen that the transmittance is quite high so only a little of the x-rays are absorbed by the gold. In the zoomed image the transmittance isn't decreasing near the K_α energy so fitting erf-function to the mass attenuation coefficients isn't possible.

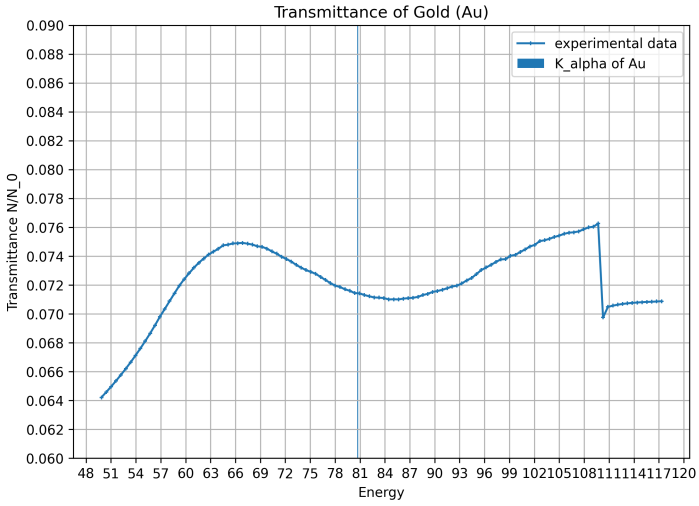

Figure 15. Transmittance of the 490 µm gold foil. The transmittance is decreasing near the K_α energy of the gold thus making it possible to fit erf-function to the mass attenuation coefficients. Note that the transmittance is quite low, near 7.5 %, over the whole energy range.

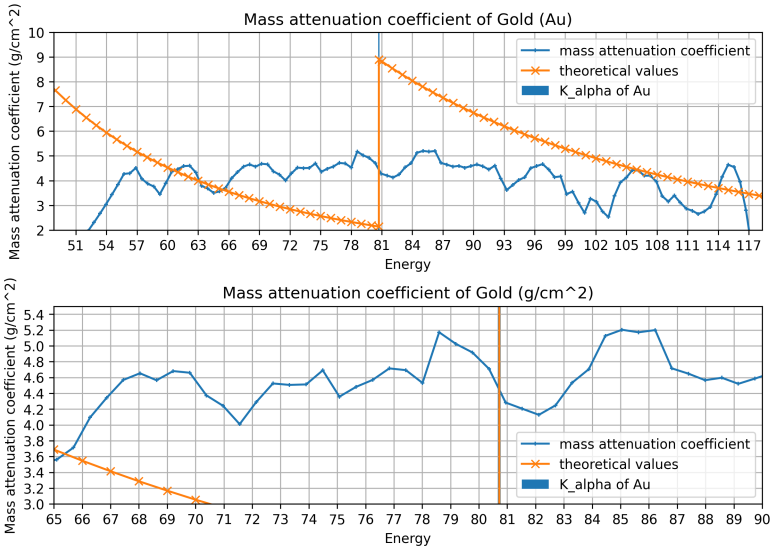

Figure 16. Mass attenuation coefficients for the 5 µm thin gold foil. Similiarly to figure 14 the mass attenuation coefficients aren't increasing near the K_α edge energy of the gold.

The direct result of this measurement is the energy resolution of 10.1784 ± 0.0052 keV for panel 3 in charge summing mode. The discrepancy found with the Americium-241 measurement most likely effects this measurement. However, in this measurement pixel-to-pixel differences were somewhat compensated because the transmittance

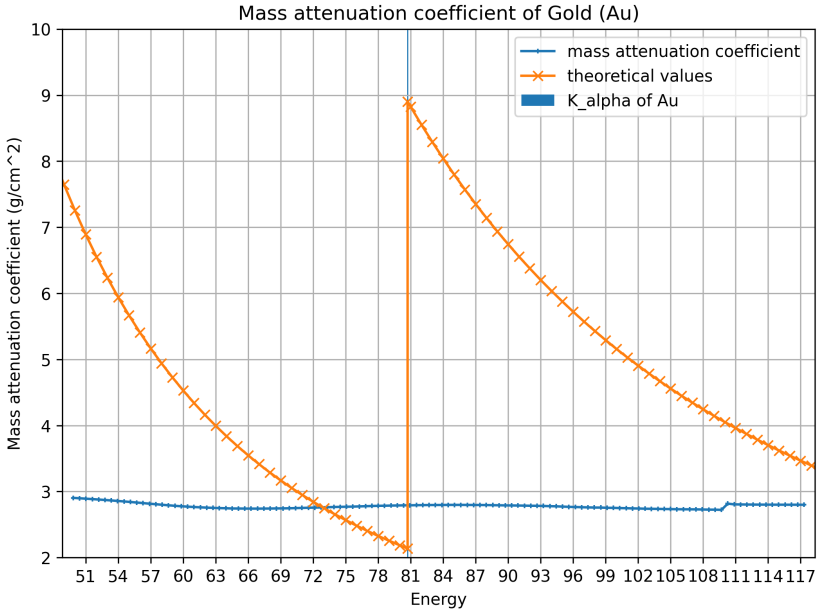

(a)

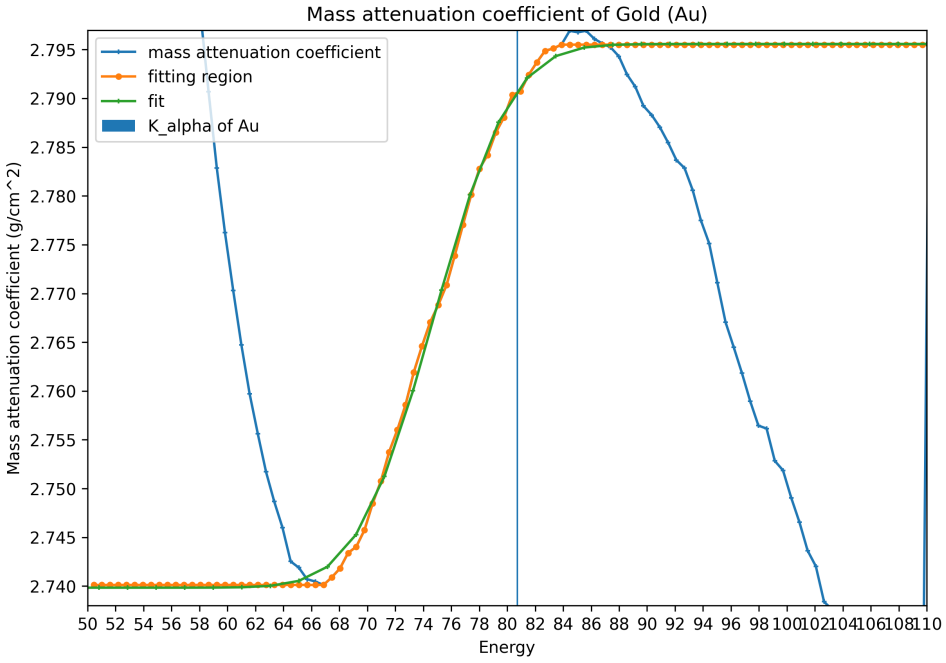

(b)

Figure 17. Mass attenuation coefficients for the 490 µm thick gold foil. From (a) It can be seen that the increase in mass attenuation coefficients doesn't quite follow the theoretical values given in [1]. However, zooming in the data the erf-function can be fitted to the K_α-edge.

was calculated using division by pixels. This division works as a simple correction to the differences between pixels. It would be interesting to see if how the FWHM behaves when the energy of the k-edge differs.

4.6 Niobium and Rhodium foil measurements

The transmittance of niobium and rhodium foils were measured the same way as gold foils with the distance from the camera to the foils being 32 cm. The K_α edges of the niobium and rhodium foils are at 18.99 keV and 23.22 keV respectively [1].

The images were taken with the camera in charge summing mode with super narrow gain. Both foils were measured at the same time with threshold 1 going from DAC value 123 to 186 with step size of 1 which means 8.5 keV to 110 keV with step size of 0.21 keV in energy units. The exposure time was same 60 s as in gold foil measurements. The threshold 0 was set to 8 keV.

The x-ray tube was setup with voltage of 50 kV and with current of 100 µA without any filters.

The transmittance and mass attenuation coefficients can be seen in figures 18a and 18b respectively for Niobium. In figures 19a and 19b, the transmittance and mass attenuation coefficients for rhodium can be seen.

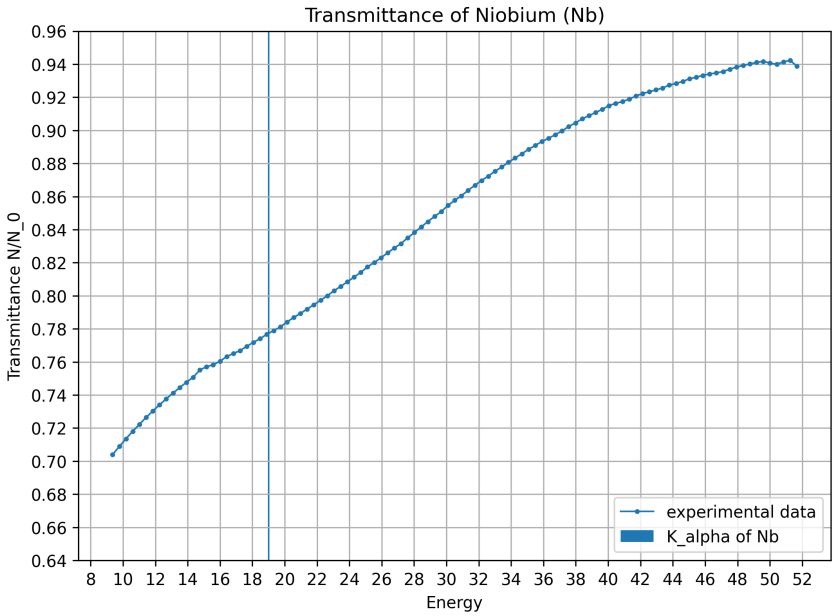

(a)

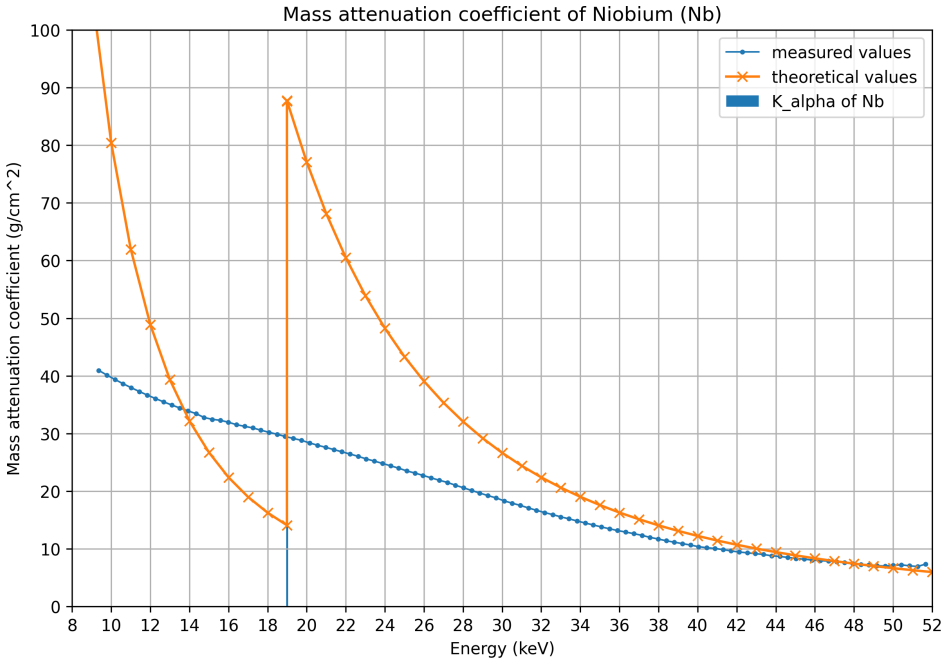

(b)

Figure 18. Transmittance and mass attenuation coefficients for the niobium foil. The transmittance (a) increases in whole energy region and thus this measurement is unusuable for fitting. The increase in transmittance results decrease in the mass attenuation coefficients (b).

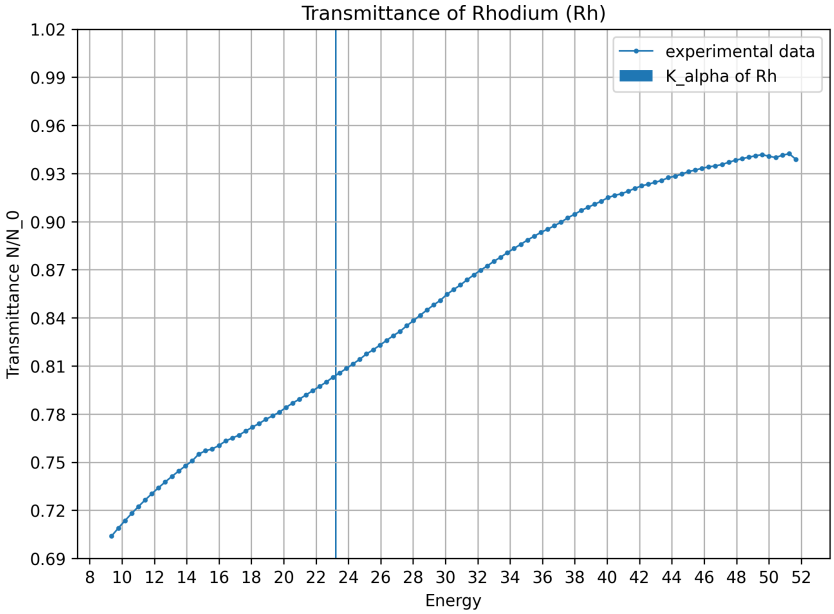

(a)

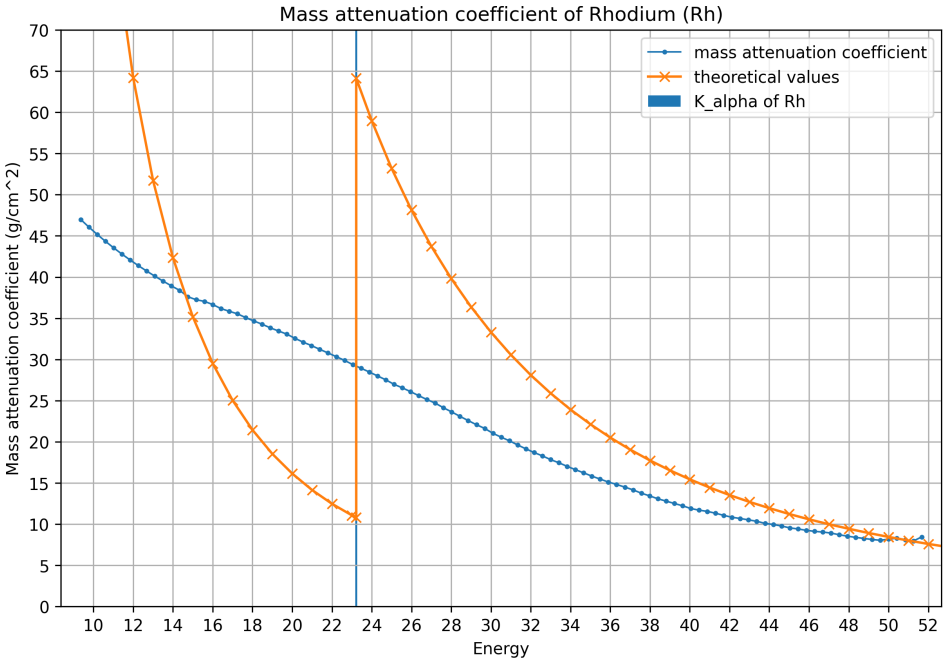

(b)

Figure 19. Transmittance and mass attenuation coefficients for the rhodium foil. Similiary to 18a and 19b the transmittance (a) increases in whole energy region which leads to decrease in mass attenuation coefficients (b).

Before the measurement, it was assumed that the K_α edges can't be distinguished from the spectrum. As per figures 18b and 19b, it turns out the K_α edges aren't visible in the spectrum. The increase in the transmittance likely confirms that internal fluorescence happens in the measured energy range. This most likely leads to the increasing transmittance.

4.7 Spatial resolution

Spatial resolution of the camera was determined by doing a slanted edge measurement. In the slanted edge measurement, a target with a straight edge is imaged. The target is rotated by a known angle in either horizontal or vertical direction and should fill half of the image the rest of the image filled by the unattenuated beam. The target should be chosen so that it passes x-rays as little as possible to maximize the contrast between the target and the unblocked beam in the images.

After the target has been imaged modulation transfer function is calculated from the images. The modulation transfer function is a measurement for how well the optical system reproduces spatial frequencies, or, quantifies the sharpness of the edge in the image.

In the case of slanted edge measurements, the modulation transfer function is the normalized magnitude of Fourier transform of the line spread function. Line spread function determines how a sharp line spreads as the function of pixels orthogonal to the line. The line spread function is the derivative of the edge spread function in a direction orthogonal to the slanted edge. Edge spread function tells how the edge spreads in the orthogonal direction to the slanted edge in the image. This process could be done without the rotated edge however rotated edge allows for better sampling of the edge as the edge can be over sampled along the rotated edge giving more statistics of the edge spread. In other words, the pixels projected to the orthogonal line are in different spots with slanted edge and thus slanted edge provides more statistics. Without slanted edge the pixels would be at a few discrete positions on the orthogonal line.

I used a lead plate that was rotated by approximately 5° as the imaging target. The edge of the lead plate was machined as even as possible and it was fixed on a 3D printed stand that was modelled to have a 5° angle but the error of the angle remains unknown. The lead target can be seen in figure 20a in position for capturing a slanted edge measurement of the first panel of the first half of the camera. These

measurements were done using a correction. The correction was done using mean of the images without the target in the beginning and at the end of the measurement. This correction was done to cancel some pixel-to-pixel variations from the slanted edge images.

In figure 20b, the lead target is in position for correction measurement at the end of the measurement for the last panel of the camera in rightmost side.

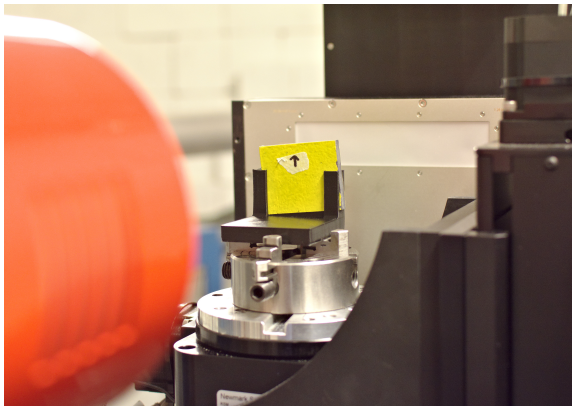

(a)

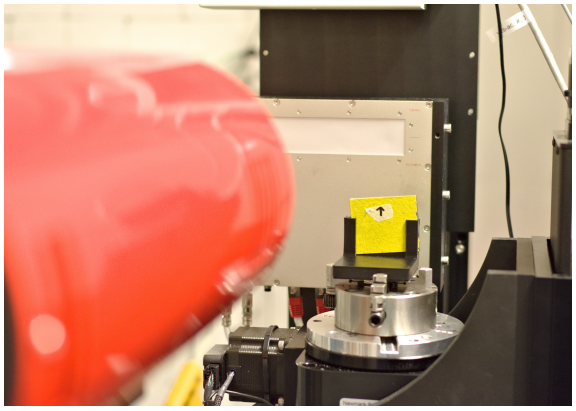

(b)

Figure 20. Measurement setup for the determination of the position resolution. In figure (a) the yellow lead target with slanted edge is in position to be imaged with the leftmost panel of the camera. In figure (b) the lead target is in position for correction image at the end of the measurement.

Position resolution was determined by loosely following the standard measurement in ISO 12233:2017. The modulation transfer function was calculated using the method described in [30]. The analysis begins from the slanted target images seen in figure 21.

Some pixels in the images had zero value which resulted in division by zero during

the correction image. These zero valued pixels had to be corrected for analysis to continue. The correction was done by taking the mean from first and second neighbours of the zero valued pixel and assigning the mean as the value of the pixel.

To construct the edge spread function the edge must be detected from the slanted target image. I determined the edge from the slanted target image that was blurred using Gaussian blur. For the edge detection I first used Otsu's thresholding method and then used edge detection on the Otsu thresholded image.

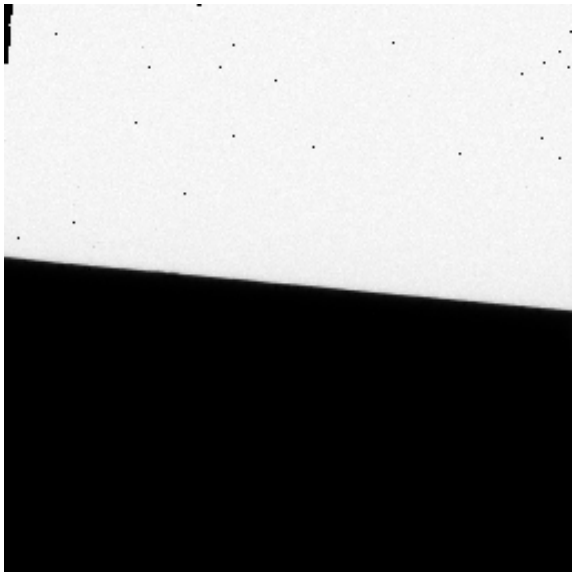

Figure 21. End result from imaging the slanted lead target with x-ray tube voltage of 120 kV with the camera in CSM mode. The imaged panel was the last panel of the D02 half. Note that there are dead pixels on the left upper corner and some dead pixels in the white region.

After the edge was detected from the slanted target image the edge spread function was constructed by projecting pixels to a line from a region of interest (ROI) covering the edge in the image. The region of interest was 16×64 pixels. The projection axis is perpendicular to the edge in the slanted target image. The ISO 12233:2017 determines a different way to reconstruct edge spread function however it only differs in the projection. The projection is done according to [30] which can be formulated mathematically as

$$z = \vec{n} \cdot (\vec{p}_{x,y} - \vec{p}_{x_0,y_0}) \tag{29}$$

where $\vec{n}$ is an unit vector perpendicular to the edge and $\{\vec{p}_{x_0,y_0}\}$ is an abitrary point

on the projection line and $\vec{p}_{x,y}$ is a point on the image. This results in points z,$i(x,y)$ for all (x,y) in which (x,y) are coordinates of the image and the $i(x,y)$ are the pixel values in the image of the slanted target. The points z,$i(x,y)$ form an approximation of the edge spread function.

The points $(z,i(x,y))$ aren't uniformly distributed and thus unsuitable for calculating modulation transfer function with fast Fourier transform. The points $(z,i(x,y))$ are processed with locally weighted scatterplot smoothing (LOWESS) to make the points uniformly distributed [30]. The LOWESS method smoothes the pixel-to-pixel differences in the panel. After LOWESS processing, the function presented by the LOWESS predictions is differentiated using local polynomial fitting at uniformly distrubuted points. The polynomial fits were done using second-degree polynomials and with the fitting window of 9 values. The differentiated function estimates the derivative of the original data. Derivative of edge spread function is line spread function mentioned earlier. The line spread function was processed with convolution of the Hamming window. The reason for using Hamming window was to fix discontinuity between the beginning and the end of the edge spread function. This method differs from the method described in [30] as there the differentation scheme isn't described thus the local fitting method was chosen. Neither is the line spread function processed using the Hamming window.

Fourier transform was then calculated from the line spread function and normalized to be in [0,1] and the x-axis was converted to units of $\frac{\text{line pairs}}{\text{mm}}$. The conversion isn't straightforward as the projection line is tilted and has to be accounted for. The conversion factor was calculated with

$$c = \frac{0.055\,\text{mm}}{sm} \cos\alpha, \tag{30}$$

where 0.055 mm is the distance between pixels, sm is the number of LOWESS predictions compared to number of pixels in the projection line and α is the angle between image's horizon and the projection line. Due to the conversion factor (30) not being constant between the the panels the data was interpolated to be with spacing

$$c_s = \frac{0.055\,\text{mm}}{sm} \tag{31}$$

which is independent of the projection line angle. The interpolation was done using PCHIP interpolation. After this the 10 % MTF point was linearly interpolated.

This measurement was done in both single pixel mode and charge summing mode for x-ray tube voltages of 40 kV with no filter, 120 kV with HE-3[3]. filter and 150 kV with HE-6 filter. The current for the tube was chosen so that the spot size of the x-ray tube would be smallest. This is possible by selecting the current so that the power is 4 W according to the manufacturer. This means that the current used for measurement with 40 kV voltage was 100 µA, with 120 kV voltage the current was 33 µA and with 150 kV voltage the current was 27 µA. The thresholds were kept constant for each mode. For single pixel mode the threshold 0 was chosen to be 10 keV and for charge summing mode the threshold 1 was similarly 10 keV and the threshold 0 was 8 keV. The distance between lead target and the camera was 91.9 mm. The distance was compromise in minimizing the geometrical magnification and fixation of the target. Fixation closer to the camera wasn't possible and thus this was minimal achievable geomterical magnification.

The 10 % MTF values are show in table 2. To further show differences between panels in different modes means and standard deviations were plotted in figs. 22a, 22b, 23a, 23b, 24a and 24b.

The position resolution is near the theoretical value of the pixel size 55 µm, which corresponds to 9.091 lp/mm, on all modes and measured energies. The halves have similiar energy resolution with similiar deviation in the panels except for measurement in CSM mode with 40 keV. The high deviation on the measurement is likely due to the panel number 5 having bad pixels in the region of interest. The bad pixels could be hot pixels or pixels with constant values. Each panel has some constant value pixels near the edge but some of these stuck pixels can be found near the center of the panel. These could be compensated using outlier removal, however, this could lead to unrealistic position resolution depending on the compensation method.

Overall the the 10 % MTF average for the whole camera over all the measured energies and panels was 9.24 lp/mm with standard deivation of 2.64 lp/mm for SPM mode. This agrees with the the pixel size of 55 µm. For the CSM mode the average was 11.35 lp/mm with standard deviation of 2.32 lp/mm. The spatial resolution is slightly better in the charge summing mode compared to the single pixel mode.

[3]The filter is made out of glass and has thickness of 2.5 mm

Chip	Measurement			
D02-W0558-5	40kV SPM	40 kV CSM	120kV HE3 SPM	120kV HE3 CSM
Panel 1	11.235	10.185	7.484	9.025
Panel 2	11.827	11.089	8.073	8.288
Panel 3	11.606	12.69	8.282	10.804
Panel 4	17.699	10.854	7.44	10.252
Panel 5	12.229	13.232	7.475	10.147
G04-W0558-5				
Panel 1	10.819	11.057	7.037	9.718
Panel 2	12.526	13.799	7.624	11.956
Panel 3	13.417	11.721	7.764	12.3
Panel 4	11.107	14.794	7.942	10.575
Panel 5	13.037	20.53	7.75	9.234

Chip	Measurement	
D02-W0558-5	150kV HE6 SPM	150kV HE6 CSM
Panel 1	7.948	9.645
Panel 2	7.497	13.709
Panel 3	7.59	10.417
Panel 4	7.26	11.865
Panel 5	7.248	9.616
G04-W0558-5		
Panel 1	6.974	10.582
Panel 2	7.904	12.126
Panel 3	7.465	9.131
Panel 4	7.289	10.154
Panel 5	7.752	11.038

Table 2. Resolution corresponding to the 10 % of modulation transfer function for each half and each panel for each measured settings. The values are in line pairs per millimeter.

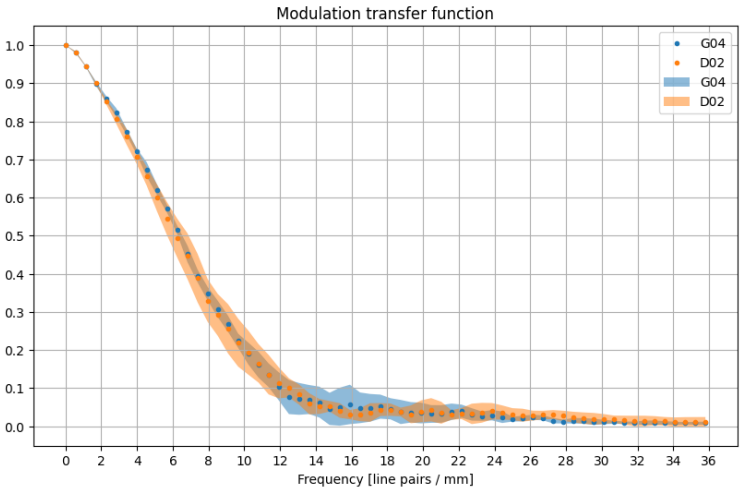

(a)

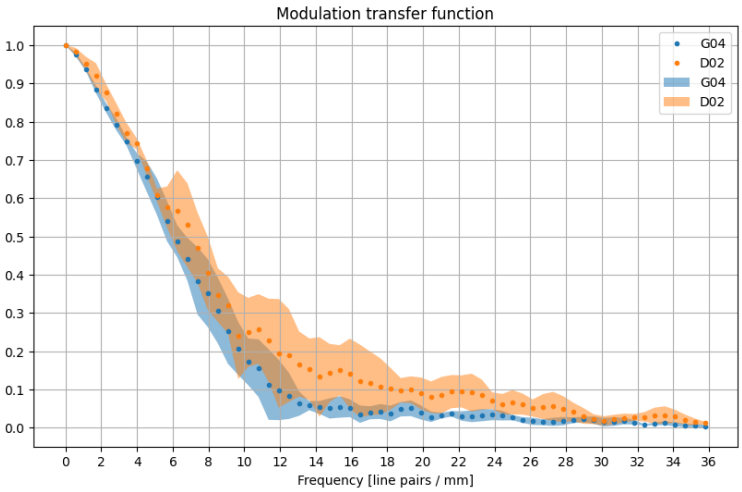

(b)

Figure 22. Modulation transfer function with x-ray tube voltage of 40 kV in single pixel mode mode (a) and in charge summing mode (b). Standard deviation from panels has been plotted as an area plot. For unknown reason, the standard deviation is quite high in CSM mode compared to SPM mode.

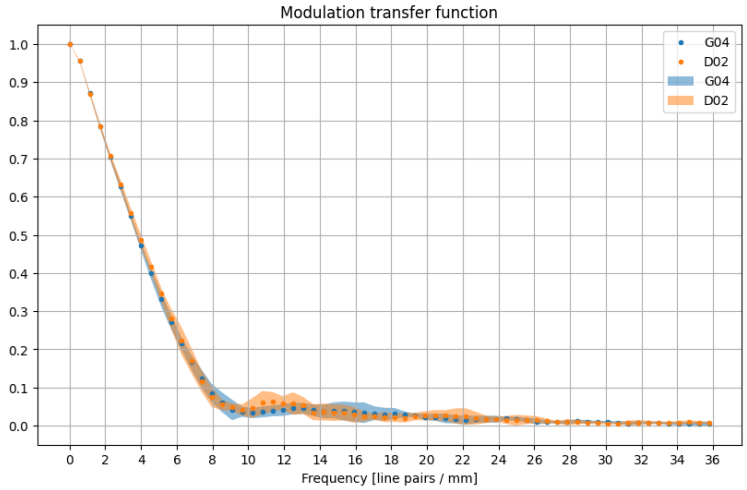

(a)

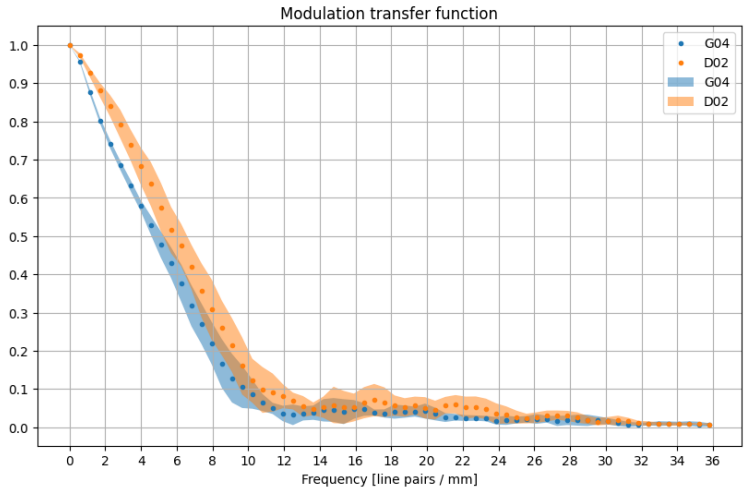

(b)

Figure 23. Modulation transfer function with x-ray tube voltage of 120 kV in SPM mode (a) and in CSM mode (b). Standard deviation from panels has been plotted as an area under type plot. Similiarly to 23b the CSM mode has slightly higher standard deviation compared to SPM mode but the difference is less compared to measurement done using x-ray tube voltage of 40 kV. The standard deivation is higher compared to 150 kV xray tube voltage.

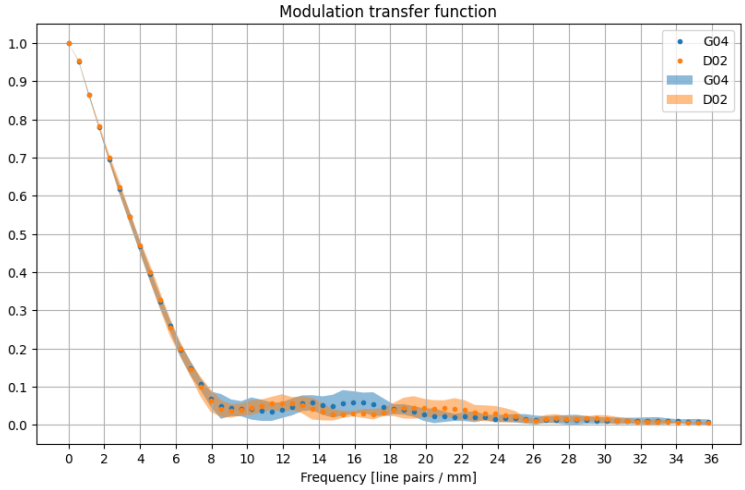

(a)

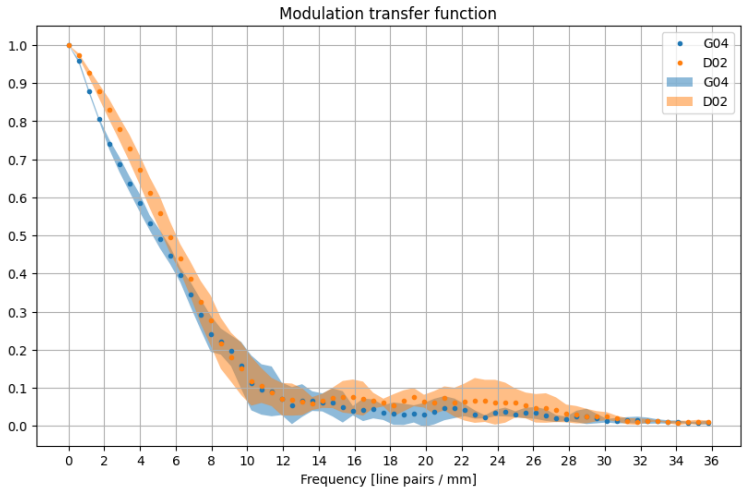

(b)

Figure 24. Modulation transfer function with x-ray tube voltage of 150 kV in SPM mode (a) and in CSM mode (b). Standard deviation from panels has been plotted as an area under type plot.

5 Conclusions

The measurements done in this thesis gives roughly the results expected from the manufacturer. The noise edge is low enough to use charge summing mode in most measurements. The safe 8 keV minimum for threshold 0 should be usable for most measurements done using this combination of x-ray tube and the Advacam.

The photon counting speed requires more research the presented way is the way not to measure it. Perhaps the measurement could have been improved by using additional filtering to reduce the minimum photon count. It remains unknown why the photon counting speed remains higher than 1 in single pixel mode with low photon fluxes but the counting speed decreases for low fluxes in charge summing mode.

Energy resolution determined using both ways is roughly the same 10 keV given by the manufacturer. However, the pixel-to-pixel differences in threshold values should be calibrated or the calibration should be checked. This checking could be done using other radioisotopes like iron-55 or other monochromatic x-ray sources. Perhaps the calibration is good in the whole energy range and the pixel-per-pixel differences are even when the whole energy range is considered. Another way to check this discrepancy could be to use mass attenuation coefficient measurements using K-edges with different energies. Obviously every panel in the camera should be measured and compared with each other as this thesis focused only on panel 3 of the D02 half.

The spatial resolution measurement gives overall reasonable resolution for the camera and its pixel size. The expection for the spatial resolution was that it is near the pixel size 55 µm and that it depends more on the energy in single pixel mode than is charge summing mode [31]. The first assumption holds but for the second assumption more measurements would be required as in [31] the measurements were done using monochromatic beam and changing the energy threshold. I had polychromatic beam and changed the voltage of the x-ray tube but didn't measure using multiple threshold values. If I had measured using multiple thresholds using multiple tube voltages the number of measurements would have been to high for the

scope of this thesis.

A lot of questions were answered but a lot of work remains to be done to fully characterize the camera. For example, to continue the work on characterizing the camera the pixel-per-pixel differences could be measured in broader energy range.

Another possibility is to continue with determination of the photon counting speed by developing a way to measure the number of incoming photons and comparing the results obtained against the results from the camera. This might be realizable by using different detector for counting the number of incoming photons, however, the geometry of the measurement makes usage of different detector hard.

If desired the spatial resolution could be determined using different x-ray tube voltages or by comparing different energy threshold with constant x-ray tube voltage. This was left out from this thesis as it was determined to be out of the scope of this thesis.

References

[1] S. Seltzer. *XCOM-Photon Cross Sections Database, NIST Standard Reference Database 8*. 1987. DOI: 10.18434/T48G6X. URL: http://www.nist.gov/pml/data/xcom/index.cfm.

[2] J. H. Hubbell et al. "Atomic form factors, incoherent scattering functions, and photon scattering cross sections". In: *Journal of Physical and Chemical Reference Data* 4.3 (1975), pp. 471–538. DOI: 10.1063/1.555523.

[3] C. Leroy and P.-G. Rancoita. *Principles of radiation interaction in matter and detection 2nd Edition*. London: World Scientific, 2009.

[4] A. H. Compton. "A Quantum Theory of the Scattering of X-rays by Light Elements". In: *Phys. Rev.* 21 (5 May 1923), pp. 483–502. DOI: 10.1103/PhysRev.21.483.

[5] R. D. Evans. *Atomic Nucleus*. McGraw-Hill, inc, 1955.

[6] G. F. Knoll. *Radiation detection and measurement; 4th ed.* New York, NY: Wiley, 2010.

[7] A. J. P. Theuwissen. *Solid-state imaging with charge-coupled devices*. New York, Boston, Dordrecht, London, Moscow: Kluwer Academic Publishers, 2002. ISBN: 0-306-47119-1.

[8] C. Kittel. *Introduction to Solid State Physics*. Wiley, 2004. ISBN: 9780471415268.

[9] F. Scholze et al. "Determination of the electron–hole pair creation energy for semiconductors from the spectral responsivity of photodiodes". In: *Nuclear Instruments and Methods in Physics Research Section A: Accelerators, Spectrometers, Detectors and Associated Equipment* 439.2 (2000), pp. 208–215. ISSN: 0168-9002. DOI: 10.1016/S0168-9002(99)00937-7.

[10] M. G. Collet. "Solid State Image Sensors". In: *Solid-State Imagers and Their Applications*. Ed. by G. J. Declerck. Vol. 0591. International Society for Optics and Photonics. SPIE, 1986, pp. 82–93. DOI: 10.1117/12.952082.

[11] M. Bigas et al. “Review of CMOS image sensors”. In: *Microelectronics Journal* 37.5 (2006), pp. 433–451. ISSN: 0026-2692. DOI: 10.1016/j.mejo.2005.07.002.

[12] T. Lule et al. “Sensitivity of CMOS based imagers and scaling perspectives”. In: *IEEE Transactions on Electron Devices* 47.11 (2000), pp. 2110–2122. DOI: 10.1109/16.877173.

[13] Hamamatsu. URL: https://www.hamamatsu.com (visited on 11/21/2021).

[14] R. Ballabriga et al. “Review of hybrid pixel detector readout ASICs for spectroscopic X-ray imaging”. In: *Journal of Instrumentation* 11.01 (Jan. 2016), P01007–P01007. DOI: 10.1088/1748-0221/11/01/p01007.

[15] S. Yoshida and T. Ohsugi. “Application of silicon strip detectors to X-ray computed tomography”. In: *Nuclear Instruments and Methods in Physics Research Section A: Accelerators, Spectrometers, Detectors and Associated Equipment* 541.1 (2005). Development and Application of Semiconductor Tracking Detectors, pp. 412–420. ISSN: 0168-9002. DOI: 10.1016/j.nima.2005.01.083.

[16] M. Sjölin and F. Grönberg. “Obtaining measurement information from an edge-on X-ray detector and determining the orientation of an edge-on X-ray detector with respect to the direction of incoming X-rays”. QC 20210610. 2018.

[17] M. O. Krause. “Atomic radiative and radiationless yields for K and L shells”. In: *Journal of Physical and Chemical Reference Data* 8.2 (Apr. 1979), pp. 307–327. DOI: 10.1063/1.555594.

[18] A. Thompson. *X-ray Data Booklet*. Lawrence Berkeley National Laboratory, University of California, 2009.

[19] D. Pennicard and H. Graafsma. “Simulated performance of high-Z detectors with Medipix3 readout”. In: *Journal of Instrumentation* 6.06 (June 2011), P06007–P06007. DOI: 10.1088/1748-0221/6/06/p06007.

[20] E. H. Heijne et al. “LHC1: A semiconductor pixel detector readout chip with internal, tunable delay providing a binary pattern of selected events”. In: *Nuclear Instruments and Methods in Physics Research Section A: Accelerators, Spectrometers, Detectors and Associated Equipment* 383.1 (1996). Development and Application of Semiconductor Tracking Detectors, pp. 55–63. ISSN: 0168-9002. DOI: 10.1016/S0168-9002(96)00658-4.

[21] M. Campbell et al. “A readout chip for a 64 × 64 pixel matrix with 15-bit single photon counting”. In: *IEEE Transactions on Nuclear Science* 45.3 (1998), pp. 751–753. DOI: 10.1109/23.682629.

[22] R. Ballabriga, M. Campbell, and X. Llopart. “An introduction to the Medipix family ASICs”. In: *Radiation Measurements* 136 (2020), p. 106271. ISSN: 1350-4487. DOI: 10.1016/j.radmeas.2020.106271.

[23] X. Llopart et al. “Medipix2: A 64-k Pixel Readout Chip With 55-??m Square Elements Working in Single Photon Counting Mode”. In: *Nuclear Science, IEEE Transactions on* 49 (Nov. 2002). DOI: 10.1109/TNS.2002.803788.

[24] X. Llopart et al. “Medipix2: A 64-k pixel readout chip with 55-µm square elements working in single photon counting mode”. In: *IEEE Transactions on Nuclear Science* 49.5 (2002), pp. 2279–2283. DOI: 10.1109/TNS.2002.803788.

[25] F. Krummenacher. “Pixel detectors with local intelligence: an IC designer point of view”. In: *Nuclear Instruments and Methods in Physics Research Section A: Accelerators, Spectrometers, Detectors and Associated Equipment* 305.3 (1991), pp. 527–532. ISSN: 0168-9002. DOI: 10.1016/0168-9002(91)90152-G.

[26] R. Ballabriga et al. “The Medipix3RX: a high resolution, zero dead-time pixel detector readout chip allowing spectroscopic imaging”. In: *Journal of Instrumentation* 8.02 (Feb. 2013), pp. C02016–C02016. DOI: 10.1088/1748-0221/8/02/c02016.

[27] V. Sriskaran et al. “New architecture for the analog front-end of Medipix4”. In: *Nuclear Instruments and Methods in Physics Research Section A: Accelerators, Spectrometers, Detectors and Associated Equipment* 978 (2020), p. 164412. ISSN: 0168-9002. DOI: 10.1016/j.nima.2020.164412. URL: https://www.sciencedirect.com/science/article/pii/S0168900220308093.

[28] R. M. Doesburg et al. “Spectrum measurement using Medipix3 in charge summing mode”. In: *Journal of Instrumentation* 7.11 (2012). DOI: 10.1088/1748-0221/7/11/c11004.

[29] B. N. L. National Nuclear Data Center. *NuDat (Nuclear Structure and Decay Data)*. Mar. 2008.

[30] K. Kohm. “Modulation transfer function measurement method and results for the Orbview-3 high resolution imaging satellite”. In: *International Archives of the Photogrammetry, Remote Sensing and Spatial Information Sciences* 35 (Jan. 2004).

[31] T. Koenig et al. “How spectroscopic x-ray imaging benefits from inter-pixel communication”. In: 59.20 (Sept. 2014), pp. 6195–6213. DOI: 10.1088/0031-9155/59/20/6195.

[32] S. Stock. *MicroComputed Tomography: Methodology and Applications, Second Edition*. CRC Press, 2019. ISBN: 9781498775014.